Universidade Estadual de Campinas

Instituto de Física *Gleb Wataghin*

Diego Salam Claro

Análise computacional de ondas dispersivas em poços preenchidos por fluidos

Computational analysis of dispersive acoustic waves in fluid-filled boreholes

campinas
2020

Diego Salam Claro

Computational analysis of dispersive acoustic waves in fluid-filled boreholes

Análise computacional de ondas dispersivas em poços preenchidos por fluidos

Dissertação apresentada ao Instituto de Física *Gleb Wataghin* da Universidade Estadual de Campinas como parte dos requisitos exigidos para a obtenção do título de Mestre em Física, na área de Física Aplicada.

Dissertation presented to the *Gleb Wataghin* Institute of Physics of the University of Campinas in partial fulfillment of the requirements for the degree of Master in Physics, in the area of Applied Physics.

Supervisor/Orientador: Odilon Divino Damasceno Couto Junior

Este exemplar corresponde à versão final da dissertação defendida pelo aluno Diego Salam Claro, e orientada pelo Prof. Dr. Odilon Divino Damasceno Couto Junior.

Campinas

2020

Ficha catalográfica
Universidade Estadual de Campinas
Biblioteca do Instituto de Física Gleb Wataghin
Lucimeire de Oliveira Silva da Rocha - CRB 8/9174

C562c

Claro, Diego Salam, 1996-
Computational analysis of dispersive acoustic waves in fluid-filled boreholes / Diego Salam Claro. – Campinas, SP : [s.n.], 2020.

Orientador: Odilon Divino Damasceno Couto Junior.
Dissertação (mestrado) – Universidade Estadual de Campinas, Instituto de Física Gleb Wataghin.

1. Modelos acústicos. 2. Geofísica. 3. Método dos elementos finitos. I. Couto Junior, Odilon Divino Damasceno, 1979-. II. Universidade Estadual de Campinas. Instituto de Física Gleb Wataghin. III. Título.

Informações para Biblioteca Digital

Título em outro idioma: Análise computacional de ondas dispersivas em poços preenchidos por fluídos
Palavras-chave em inglês:
Acoustic models
Geophysics
Finite element method
Área de concentração: Física Aplicada
Titulação: Mestre em Física
Banca examinadora:
Odilon Divino Damasceno Couto Junior [Orientador]
Ricardo Leiderman
Alexandre Fontes da Fonseca
Data de defesa: 31-08-2020
Programa de Pós-Graduação: Física

Identificação e informações acadêmicas do(a) aluno(a)
- ORCID do autor: https://orcid.org/0000-0002-9272-1950
- Currículo Lattes do autor: http://lattes.cnpq.br/9339714348790302

MEMBROS DA COMISSÃO JULGADORA DA DISSERTAÇÃO DE MESTRADO DE **DIEGO SALAM CLARO - RA 155168** APRESENTADA E APROVADA AO INSTITUTO DE FÍSICA "GLEB WATAGHIN", DA UNIVERSIDADE ESTADUAL DE CAMPINAS, EM 31 / 08 / 2020.

COMISSÃO JULGADORA:

- Prof. Dr. Odilon Divino Damasceno Couto Junior – Orientador – DFMC/IFGW/UNICAMP
- Prof. Dr. Ricardo Leiderman – IC/UFF
- Prof. Dr. Alexandre Fontes da Fonseca – DFA/IFGW/UNICAMP

OBS.: Ata de defesa com as respectivas assinaturas dos membros encontra-se no SIGA/Sistema de Fluxo de Dissertação/ Tese e na Secretaria do Programa da Unidade.

CAMPINAS
2020

Ao verme que primeiro roerá
as frias carnes do meu cadáver
dedico como saudosa lembrança
~~estas memórias póstumas~~ esta dissertação.

Adaptado de: ASSIS, Machado de. Memórias póstumas de Brás Cubas

Agradecimentos

Agradeço aos meus pais e irmãos por todo apoio e compreensão ao longo da gradução e do mestrado.

A TODOS os meus amigos que contribuiram de forma direta ou indireta para conclusão deste trabalho. Também ao pessoal do GPO e do GFNMN pelos cafés e conversas jogadas fora.

Ao Prof. Dr. Pablo Diniz Batista e ao Prof. Dr. Tobias Heimfarth pelos códigos cedidos e pelas frutíferas discussões ao longo do projeto. Aos Profs. Drs. Fanny Béron, Gustavo Wiederhecker, Thiago Alegre, Francisco Rouxinol, Alexandre Fontes da Fonseca e Ricardo Leiderman pelas idéias, questionamentos e apontamentos feitos para melhorar a qualidade do trabalho.

Agradeço ao meu orientador pela paciência, correções e ensinamentos que perpassam os adquiridos sobre o tema.

Ao IFGW, FUNCAMP e Unicamp pelas estruturas fornecidas.

À Petrobras (Petróleo Brasileiro S.A: 5900.0111052.19.9 – SAP 4600586013) e o CNPq (135915/2018-0) pelo financiamento. Também a equipe da Petrobras que nos acompanhou de perto. Em especial aos pesquisadores Douglas L. P. de Lacerda e Carlos F. Beneduzi pelas discussões.

Resumo

Neste trabalho, usamos o Método dos Elementos Finitos (MEF) para estudar a propagação de modos acústicos em um poço infinito preenchido por fluido e cercado por um sólido homogêneo e isotrópico. Primeiramente, usando uma aproximação bidimensional (2D) no plano transversal do poço, um modelo de análise modal foi proposto. Discutimos a distribuição geométrica, interpretação física e obtivemos as curvas de dispersão dos principais modos propagantes: Stoneley, flexural e quadrupolar. Os resultados foram validados por comparação direta com a solução analítica e numérica disponíveis na literatura. Após isso, analisamos o problema no domínio do tempo usando uma aproximação no plano longitudinal. Utilizamos o MEF para simular a aquisição de sinais por uma ferramenta de perfilagem composta por uma fonte de monopolo com N detectores igualmente espaçados. Os resultados foram validados aplicando processos de pós-processamento de sinais, como o *Slowness Time Coherence* (STC) e o *Phase-based Dispersion Analysis* (PBDA), para obter as curvas de dispersão dos modos. Isso nos permitiu demonstrar a equivalência de nossas análises modal e temporal. Nas duas formulações, analisamos a propagação de ondas em formações rápidas e lentas, dando atenção ao caso para o limite a baixas frequências. Demonstramos que nosso modelo pode ser efetivamente útil na interpretação de dados de baixa relação sinal-ruído e também pode ser expandida para estudar sistemas mais complexos.

Palavras-chave: Perfilagem sônica, Poços preenchidos por fluido, Geofísica; Método dos Elementos Finitos.

Abstract

In this work, we use the Finite Element Method (FEM) to study the propagation of acoustic modes in an infinite fluid-filled borehole surrounded by a homogeneous and isotropic solid. First, using a two-dimensional (2D) approach in the transverse plane of the borehole, we carry out a modal analysis of the problem. We discuss the geometric distribution, physical interpretation, and obtain the dispersion curves of the main propagating modes, namely, the Stoneley, flexural, and quadrupole modes. The results are validated by direct comparison with analytical and numerical solutions available in the literature. Second, we analyze the time domain problem with a two-dimensional approximation in the borehole longitudinal plane. We use the FEM interface to simulate the signal acquisition of a logging tool composed of a monopole source with N equally spaced detectors. The results are validated by applying data post-processing methods, like the *Slowness Time Coherence* (STC) and *Phase-Based Dispersion Analysis* (PBDA), to obtain the dispersion curves of the modes. This allows us to demonstrate the equivalence of our modal and temporal analysis. In both approaches, we analyze the wave propagation in fast and slow formations, paying particular attention to the low frequency limit. We showed that our simulation model can be effectively helpful in the interpretation of low signal-to-noise experimental data and also be expanded to study more complex systems.

Keywords: Sonic logging; Fluid-filled boreholes; Geophysics; Finite Element Method.

List of figures

Contents

Chapter 1

Introduction

The main goal of geophysical experiments is to provide an accurate classification of the soil, rock, and the surrounding environment. Various experiments are conducted to gather different and needed information for mining, water management, and oil-and-gas companies. Properties such as porosity, anisotropies, and rock permeability are primarily important in petrophysical systems since they indicate the presence of hydrocarbons reservoirs. There are different types of studies based on electrical, acoustic, and nuclear measurements that are conducted for soil and subsoil classifications. [1]

In this scenario, acoustic wave propagation phenomena are broadly employed. Sonic logging is a technique based on measurements of propagating and scattered acoustic modes in a cylindrical waveguide filled with fluid and surrounded by a rock formation. The measurement probe (sonic tool) is constituted by a source of acoustic waves and an array of equally spaced detectors. The source generates an energy pulse that propagates in the system and is collected by the array detector along the borehole depth. The most commonly used sources are monopole and dipole. In monopole sources, the generated waves have an isotropic energy distribution. In dipole sources, energy is distributed in a preferential axis. The characterization of the formation is made using inversion techniques, which consist in the estimation of physical parameters (elastic constants, porosity, etc) from the compressional (P) and shear (S) wave velocities obtained after processing of the time-recorded signals [2, 3]. All inversion techniques employ the wave dispersion relation, meaning the relation between its wavenumber and wavefrequency. [4, 5]

One of the main problems in sonic logging is the reliability of the low-frequency regime of the experimentally obtained dispersion curves of some modes due to the low signal-to-noise ratios. Porosity and permeability effects tend to contribute to signal attenuation in this frequency regime [6]. Moreover, in slow formations, where the formation shear velocity is lower than the fluid compressional velocity, the formation shear wave detection after excitation with a monopole source is considerably suppressed. Quadrupole and dipole sources are usually employed to mitigate the problem. Over the last decades, an effort has been devoted to develop sophisticated numerical data processing techniques to

improve signal-to-noise ratios in the processed data and to separate the contribution of the different dispersive and non-dispersive modes which are present in the acquired signal [2, 3, 7]. However, besides the remarkable progress, analytical and numerical simulations remain essential to support the data treatment and estimate the shear wave velocity in the low-frequency regime [8].

The analytical approach is usually based on calculations using the modal matrix formalism of the elasticity theory to derive analytical expressions for simplified cases, such as wave propagation in homogeneous and isotropic solids, and obtain the dispersion curves and the signal amplitude at each detector [9–11]. Numerical approaches take place to investigate more complex and realistic situations, such as anisotropies, tool presence, and stressed solids [12, 13]. Various numerical approaches have been used: semi-analytical method [14], finite difference method [15], and finite element method (FEM) [16–21]. The advantage of FEM is its ability to treat geometrically more complex problems in comparison to semi-analytical and finite difference methods.

1.1 Organization of the dissertation

This dissertation aims to contribute to the comprehension of the physical concepts involved in wave propagation phenomena in isotropic and homogeneous fluid-filled boreholes. In particular, we are interested in the low-frequency response of dispersive modes detected in field data. To do so, we implement a FEM calculation platform which allows us to treat the problem in the time and frequency domains and that has the potential to be used in more complex situations.

Chapter 2 begins by addressing the fundamental concepts of elasticity theory necessary to the understanding of the sonic logging technique. We explore the measurement procedure and its relation to the main propagating acoustic modes of the formation. We review the fundamentals of elastic wave propagation and apply the elasticity theory to the case of fluid-filled boreholes in isotropic and homogeneous media. We discuss the general form of the solutions and their implications to the cases of fast and slow formations.

In Chapter 3, we numerically analyze the normal modes which propagate in fast and slow formations. To do so, we implemented, tested, and validated our FEM simulations in the frequency domain. The implemented model considers an infinite, homogeneous, and isotropic solid. We focus on the Stoneley, flexural, and screw (quadrupole) modes. We analyze their spatial distribution, dispersion, and propagation characteristics. We also demonstrate very good agreement of our numerical results with analytical and other numerical solutions. In particular, we show that our FEM model provides reliable dispersion curves up to at least 200 Hz, which is up to one order of magnitude lower than what is achieved with other numerical methods or in post-processed real data.

In Chapter 4, we simulate the problem in the time domain in order to mimic a real

experiment. We simulate a fluid-filled borehole surrounded by the formation. After optimizing the model, we generate a data-set which is the time response of the detector array, exactly as in the experimental situation. Then, the data undergoes post-processing treatment with two independent algorithms: Slowness Time Coherence (STC), which is a numerical method to obtain formation S and P velocities of non-dispersive modes, and Phase-based Dispersion Analysis (PBDA), which does the same for the dispersive modes. Again, we treat the case of fast and slow formations. The results are compared with the analytical solutions and our modal analysis from Chapter 3, demonstrating very good agreement in the determination of the formation shear velocity from the different approaches. Moreover, the equivalence between our FEM frequency and time-domain approaches allows us to use our model to improve the efficiency and implementation of data processing algorithms like the PBDA.

In Chapter 5, we summarize the main results of our simulations and comment on future perspectives.

Chapter 2

Sonic logging

The determination of the elastic parameters of a solid formation is important for reservoir characterization. While there are different ways to determine these parameters using wave propagation phenomena, the acoustic logging technique is one of the main disciplines in geophysical well logging [1]. This technique is used to determine the rock characteristics from the response to a pressure pulse emitted by a source and obtain the dispersion curve of the propagating waves. [8]

A tool is inserted in a fluid-filled borehole surrounded by the formation. The structure of the logging tool varies depending on the application or manufacturer. Figure 2.1(a) shows an example of a modern tool used in field data collection by Schlumberger. It is composed of 13 (R1 to R13) equally spaced (15.16 cm) detectors, sources, and acoustic insulation. One can see the presence of five different sources: MU, ML, M, Dx, and Dy. MU and ML are cylindrical ceramic monopole sources used in the measurement procedure of near propagating waves at around 8 kHz. M represents a cylindrical ceramic monopole source used for measurements of P and S waves at high-frequencies and Stoneley wave at low-frequency. Dx and Dy are dipole sources which are perpendicularly oriented. Between the far sources and receivers, there is acoustic insulation used to minimize the wave propagation inside the tool. Figure 2.1(b) shows a cross-section scheme in one detector of the receiver array. Actually, each receiver is another array composed of eight detectors azimuthally distributed. This configuration is used to detect waves propagating in different orientations, for example, the flexural modes propagating along the x and y-axis of an anisotropic formation.

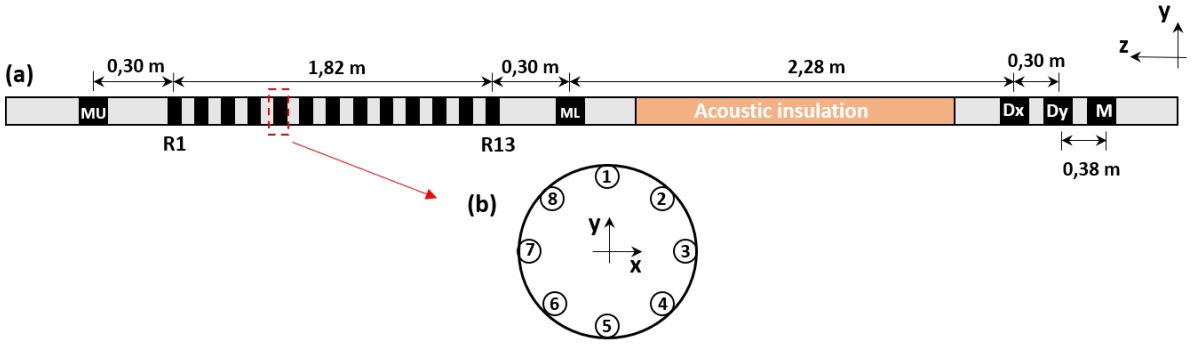

Figure 2.1: Logging tool scheme provided by Schlumberger: (a) shows the geometric parameters of the tool as well as the sources and receivers positions; (b) shows the azimuthal distribution of the detectors in every single detector. Adapted from [22]

.

Three types of sources are used: the monopole, dipole, and quadrupole. The monopole source emits energy isotropically. The dipole source emits energy in a preferred direction. The quadrupole source emits energy in two perpendicular directions. Usually, the emitted pulse is composed of frequencies from 0.5 Hz to 20 Hz.

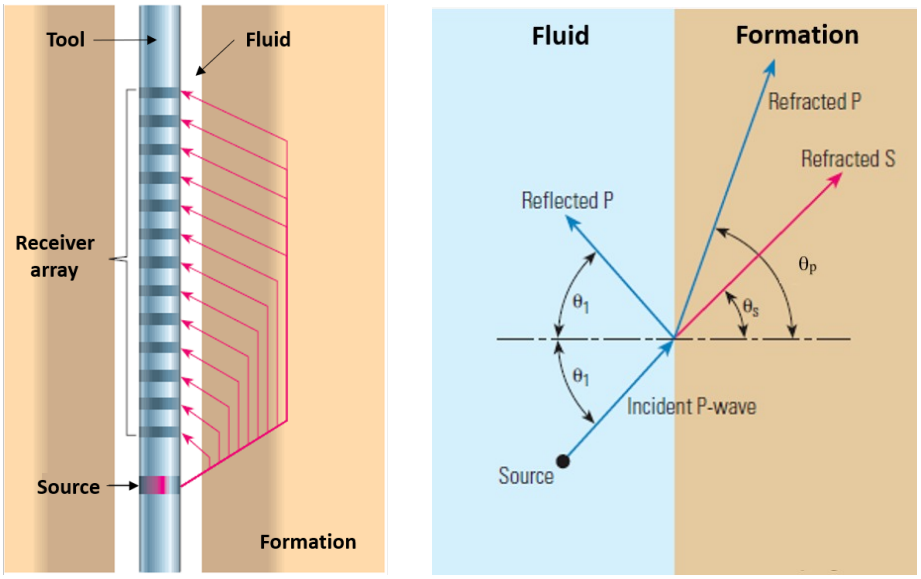

(a) (b)

Figure 2.2: (a) Sonic logging technique illustration. The upper part shows the receiver array of equally spaced detectors. The lower part shows the source. Between the tool and the formation, there is fluid. (b) Ray tracing for a fast formation. The incident wave, from the fluid, meets the borehole boundary giving rise to reflected and refracted waves with different angles at the interface. Adapted from [4].

The source emits a pulse which propagates in the fluid and then meets the borehole wall, giving rise to reflected and transmitted waves. Figure 2.2(a) shows an example of the physical situation. The transmitted wave splits into shear (v_s) and compressional (v_p) waves with different velocities. The ray tracing approximation can be used to visualize this situation, as shown in Figure 2.2(b).

The surrounding formation is usually called fast or slow. Fast formation happens when the solid shear velocity is greater than the compressional velocity of the fluid. Slow formation happens in the opposite situation: the shear velocity of the solid is lower than the compressional velocity of the fluid. Using Figure 2.2(b) and Snell's Law to relate the reflected and refracted wave angles and the velocities we get

$$\frac{\sin(\theta_1)}{\sin(\theta_p)} = \frac{v_f}{v_p} \tag{2.0.1}$$

$$\frac{\sin(\theta_1)}{\sin(\theta_s)} = \frac{v_f}{v_s} \tag{2.0.2}$$

where v_f, v_p and v_s are the fluid, compressional, and shear velocities, respectively. θ_1 is the incident angle, θ_p and θ_s are the refracted angles of each body wave. There is a certain value of θ_1, for each type of solid wave, that allows the wave propagation along the fluid-solid interface. In the slow formation ($v_s > v_f$) there is no θ_1 that satisfies this condition. In this situation, the detection of the shear wave by the detector array is considerably hindered.

Besides the compressional and shear waves in the solid, there are also interface waves that are guided along the borehole fluid-solid interface. Different sources excite different interface waves. The monopole source excites the Stoneley wave. The dipole source excites mainly the flexural wave. The quadrupole source excites the quadrupole wave. These waves are usually dispersive, the phase velocity is dependent on the frequency.

Figure 2.3 shows the experimentally recorded signals excited with a monopole source by eight equally spaced detectors: fast (Figure 2.3(a)) and slow formation (Figure 2.3(b)). For the fast formation, it is possible to see three different arrivals: the compressional, shear, and Stoneley. For slow formation, it is possible to see only the P and the Stoneley arrival, as expected from equation 2. [5]

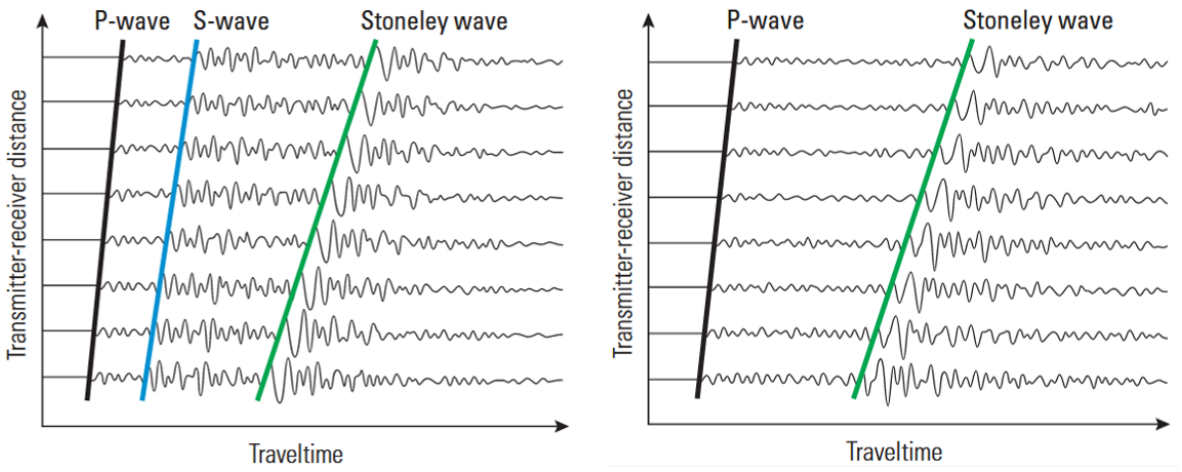

(a) (b)

Figure 2.3: Waveforms recorded by eight equally spaced detectors for (a) fast and (b) slow formation. In the fast formation, it is possible to see the presence of the compressional, shear, and Stoneley waves. In the slow formation, it is possible to see only the presence of the compressional and Stoneley waves. The arrival at each detector is illustrated with lines in different colors. Adapted from [5].

The dipole source was introduced to overcome limitations in the determination of shear velocity in slow formations using a monopole source. The dipole source excites the flexural wave which is dispersive. In the low-frequency range, the phase velocity of the flexural wave is equal to the shear velocity of the formation [23]. Therefore, obtaining the dispersion curve of the flexural wave is, in principle, a way to obtain the shear wave velocity in a slow formation. However, at low frequencies, flexural waves also have low energy and signal competes with noise.

Figure 2.4 shows the pattern of each interface mode propagating along the z-direction. In Figure 2.4(a) , on the left we show the cross-section of the tube when the Stoneley mode is propagating. The plus (+) sign indicates expansion, while the minus sign (-) indicates a compression. One can see that this mode does not have a preferred orientation, in contrast to the flexural mode shown in Figure 2.4(b) where energy is concentrated along one of the in-plane axes. The quadrupole mode in Figure 2.4(c) has two perpendicular directions, one which suffers a compression and the other an expansion.

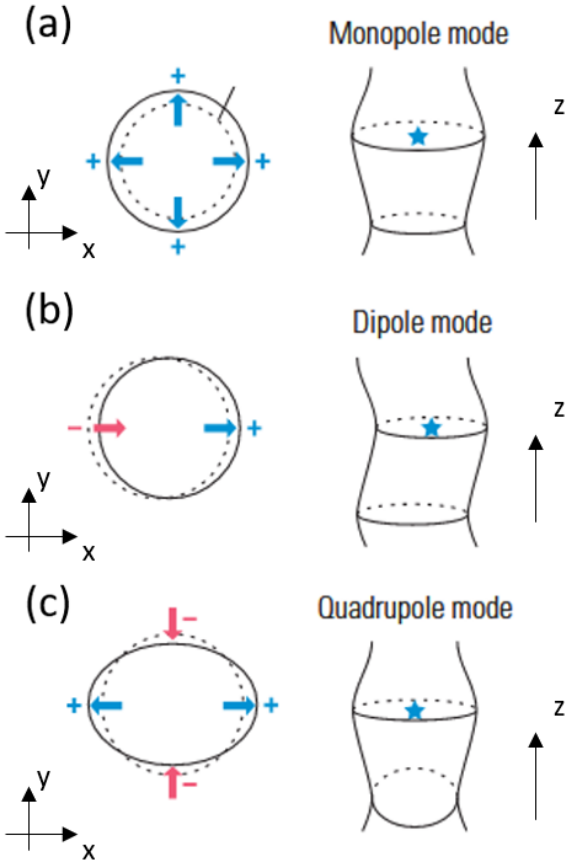

Figure 2.4: Geometrical representation of three main propagating modes: (a) Stoneley (b) Flexural (c) Screw. On the left, we show the cross-section of the tube, in which plus sign represents expansion, and the minus sign represents compression. On the right, the shape of interface mode propagating along z-direction is shown. Each one is mainly excited by a specific source. Adapted from [5].

2.1 Wave propagation

The first analytical solution for an ideal fluid-filled borehole was obtained by Biot, who explored the axisymmetric waves generated by a monopole source in a borehole surrounded by an isotropic and homogeneous medium [9]. He obtained the dispersion curve for the Stoneley wave and its asymptotic velocity in the low-frequency range. His work is considered a milestone in this research field and has been extended and complemented since his early publication.

The results for higher-order modes were gathered by Tang in 2004 [8]. Here, we follow his considerations to discuss the ideal fluid-filled borehole case. To obtain the propagating modes, we first deduce the equation of motion and then apply the boundary conditions of the system. Continuum mechanics is used along the discussion. It means that the

discrete nature of matter can be ignored and its properties are described using continuous functions. Here, we explore the key concepts involved in wave propagation.

2.1.1 Strain tensor

When a solid undergoes external forces, there will be deformation and restoring forces. The strain is a measurement of how much the medium is deformed with respect to its initial condition.

Consider two neighboring points inside an arbitrary volume V located at $P = P(\mathbf{x})$ and $Q = Q(\mathbf{x} + d\mathbf{x})$. Then, the volume V is deformed to a new configuration V'. The new location of the points are $P' = P'(\mathbf{x} + \mathbf{u}(\mathbf{x}))$ and $Q' = Q'(\mathbf{x} + d\mathbf{x} + \mathbf{u}(\mathbf{x} + d\mathbf{x}))$, where $\mathbf{u}(\mathbf{x})$ is the displacement vector. The difference between the distances of the deformed, $\overline{P'Q'}$, and non-deformed, $\overline{PQ}$, neighboring points is given by [24]

$$\begin{aligned}
\overline{P'Q'}^2 - \overline{PQ}^2 &= \sum_i \left(dx_i + u_i(\mathbf{x} + d\mathbf{x}) - u_i(\mathbf{x})\right)^2 - dx_i^2 \\
&= \sum_{k,j} \left[\left(\frac{\partial u_k}{\partial x_j} + \frac{\partial u_j}{\partial x_k} \right) + \sum_i \frac{\partial u_i}{\partial x_j} \frac{\partial u_i}{\partial x_k} \right] dx_j dx_k \\
&= \sum_{k,j} 2E_{jk} dx_j dx_k
\end{aligned} \tag{2.1.1}$$

where

$$E_{jk} = \frac{1}{2} \left[\frac{\partial u_k}{\partial x_j} + \frac{\partial u_j}{\partial x_k} + \sum_i \frac{\partial u_i}{\partial x_j} \frac{\partial u_i}{\partial x_k} \right] \tag{2.1.2}$$

It can be shown that E_{jk} is a symmetric second-order tensor and it is known as Strain Tensor. Considering small deformations, i.e., $\left|\frac{\partial u_i}{\partial x_j}\right| \ll 1$, terms of second order can be neglected, so

$$e_{jk} = \frac{1}{2} \left[\frac{\partial u_k}{\partial x_j} + \frac{\partial u_j}{\partial x_k} \right] \tag{2.1.3}$$

where e_{jk} is known as infinitesimal strain tensor, which is a symmetric linear second-tensor rank. The strain represents the relative deformation of the solid that has undergone a deformation.

2.1.2 Stress tensor

To introduce the stress tensor, we will analyze the internal forces in a solid divided into two portions separated by an imaginary surface. Consider a body divided into two parts I and II by surface A, which is oriented by $\mathbf{n}$. Part II exerts a force in part I, as shown in Figure 2.5. The stress in a given point is defined by the limit

$$\mathbf{T}(\mathbf{n}) = \lim_{\delta A \to 0} \frac{\delta \mathbf{F}}{\delta A} \tag{2.1.4}$$

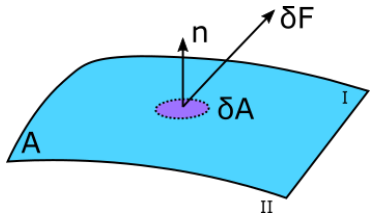

Figure 2.5: Representation of an imaginary surface A which divides the solid into two parts. $\delta\mathbf{F}$ is the force exerted by part II on part I in the area δA. The infinitesimal area is oriented by $\mathbf{n}$.

The force components which are not parallel to $\mathbf{n}$ give rise to shear tensions. The full description of the state of stress can be represented using a second-rank tensor, see [25]. So, it is defined by nine quantities

$$\sigma_{ij} = T_i(n_j) \tag{2.1.5}$$

where $T_i(n_j)$ is the i-th component of stress that acts on the normal plane with n_j orientation. This way

$$T_i = \sum_j \sigma_{ij} n_j \tag{2.1.6}$$

The stress tensor can be represented using matrix form, where the diagonal terms represent the normal stresses and the non-diagonal terms the shear stresses. Figure 2.6 represents the components of the stress tensor in the Cartesian coordinate system (x_1, x_2, x_3). The normal and shear stresses are represented using red and black colors, respectively.

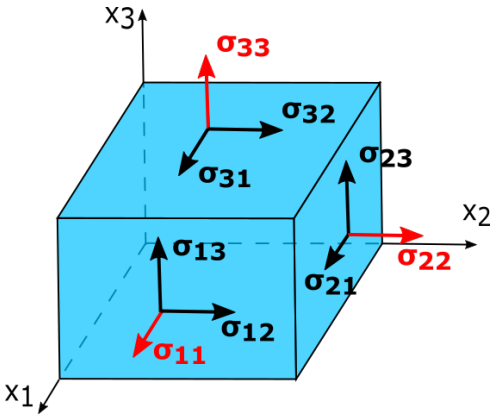

Figure 2.6: Representation of stress tensor components. Normal stresses are represented in red. Shear components are represented in black.

2.1.3 Generalized Hooke's law

A medium is called elastic if there is restoring stress which is linearly related to the strain. The major part of Hooke's observations were involving springs. Cauchy generalized the theory to elastic solids by proposing, in modern notation, the following constitutive relation between strain and stress [25]

$$\sigma_{ij} = \sum_{kl} C_{ijkl} e_{kl} \tag{2.1.7}$$

where C_{ijkl} is the element of a fourth-rank tensor known as stiffness tensor and it has 81 components, but it can be reduced to 21 independent components due to the symmetry of σ_{ij}, e_{kl}, and thermodynamics consideration [26]. The symmetries involving the stiffness tensor are

$$\begin{aligned} C_{ijkl} &= C_{jikl} \\ C_{ijkl} &= C_{ijlk} \\ C_{ijkl} &= C_{klij} \end{aligned} \tag{2.1.8}$$

Consequently, without losing generality, the stiffness tensor can be represented using the Voigt notation

$$\begin{matrix} ij \to \alpha \\ kl \to \beta \end{matrix} \quad \to \quad \begin{cases} 11 \to 1 & 32 = 23 \to 4 \\ 22 \to 2 & 31 = 13 \to 5 \\ 33 \to 3 & 12 = 21 \to 6 \end{cases} \tag{2.1.9}$$

Using the Voigt notation we can rewrite the constitutive relation using matrix notation as follows

$$\begin{bmatrix}\sigma_1\\ \sigma_2\\ \sigma_3\\ \sigma_4\\ \sigma_5\\ \sigma_6\end{bmatrix} = \begin{bmatrix} C_{11} & C_{12} & C_{13} & C_{14} & C_{15} & C_{16} \\ & C_{22} & C_{23} & C_{24} & C_{25} & C_{26} \\ & & C_{33} & C_{34} & C_{35} & C_{36} \\ & & & C_{44} & C_{45} & C_{46} \\ & Sym. & & & C_{55} & C_{56} \\ & & & & & C_{66} \end{bmatrix} \begin{bmatrix} e_1\\ e_2\\ e_3\\ 2e_4\\ 2e_5\\ 2e_6\end{bmatrix} \tag{2.1.10}$$

The stiffness tensor representation can be simplified taking into account some symmetries of the medium. The medium is called isotropic when all orientations are equivalent and, then, the stiffness tensor can be reduced using only two independent parameters as follows

$$C_{ijkl} = \lambda\delta_{ij}\delta_{kl} + \mu(\delta_{ik}\delta_{jl} + \delta_{il}\delta_{jk}) \tag{2.1.11}$$

where δ_{ij} is the Kronecker Delta, and μ and λ are referred to as Lamé's first and second parameter, respectively. Using the Voight notation, the isotropic stiffness tensor can be represented by

$$\begin{bmatrix} \lambda+2\mu & \lambda & \lambda & 0 & 0 & 0 \\ & \lambda+2\mu & \lambda & 0 & 0 & 0 \\ & & \lambda+2\mu & 0 & 0 & 0 \\ & & & \mu & 0 & 0 \\ & Sym. & & & \mu & 0 \\ & & & & & \mu \end{bmatrix} \tag{2.1.12}$$

Therefore, the stress tensor components can be written in Voigt notation as

$$\sigma_{ij} = \lambda\left(\sum_k e_{kk}\right)\delta_{ij} + 2\mu e_{ij} \tag{2.1.13}$$

2.1.4 Equation of motion

Consider a volume V with density $\rho(\mathbf{x})$ enclosed by a surface ∂A. This volume is submitted to an external force (per unit volume) $\mathbf{f}(\mathbf{x}, t)$ and a stress on the surface. Each component of the displacement vector can be written using the Newton second law and

the divergence theorem as follows [25]

$$\begin{aligned}\frac{\partial}{\partial t}\int_V \rho\frac{\partial u_i}{\partial t}dV &= \int_V f_i(\mathbf{x},t)\,dV + \int_{\partial A} T_i(\mathbf{n})dS \\ &= \int_V \left[f_i(\mathbf{x},t) + \sum_j \frac{\partial \sigma_{ji}}{\partial x_j}\right]\,dV\end{aligned} \tag{2.1.14}$$

Since V is an arbitrary volume, the following equation needs to be satisfied

$$\rho\frac{\partial^2 u_i}{\partial t^2} - f_i - \sum_j \frac{\partial \sigma_{ji}}{\partial x_j} = 0 \tag{2.1.15}$$

Using the constitutive relation for linear medium given by equation 2.1.13, the elastodynamic equation is obtained

$$\rho\frac{\partial^2 u_i}{\partial t^2} = f_i + \sum_{jkl}\frac{\partial}{\partial x_j}\left(C_{ijkl}\frac{\partial u_k}{\partial x_j}\right), \quad i = 1,2,3 \tag{2.1.16}$$

For a linear and isotropic solid, the constitutive relation 2.1.11 can be applied to equation 2.1.16. Then, the elastodynamic equation can be written as

$$\rho\frac{\partial^2 \mathbf{u}(\mathbf{x},t)}{\partial t^2} = (\lambda+\mu)\nabla(\nabla\cdot\mathbf{u}(\mathbf{x},t)) + \mu\nabla^2\mathbf{u}(\mathbf{x},t) + \mathbf{f} \tag{2.1.17}$$

Equation 2.1.17 describes the wave propagation in an elastic and isotropic solid. Various types of waves can be described using this equation and the solution may depend on the boundary conditions. Two different waves can be identified in unbounded media, the compressional and shear waves. In the first one, the displacement vector points in the same direction of the wave propagation. In the shear wave, the displacement vector is perpendicular to the direction of the wave propagation. Their values depend on the elastic parameters of the solid through the relation (see Appendix A)

$$v_p = \sqrt{\frac{\lambda+2\mu}{\rho}} \quad and \quad v_s = \sqrt{\frac{\mu}{\rho}} \tag{2.1.18}$$

From these equations, we can observe that the compressional wave velocity is always larger than shear wave velocity. Moreover, for a fluid medium, the Lame's second parameter is zero ($\mu = 0$), implying the absence of shear acoustic waves.

2.2 Fluid-filled boreholes

In a fluid-filled borehole, the presence of the liquid-solid interface creates a waveguide and leads to the appearance of other propagating modes apart for the unbound ones. However, since we are dealing with isotropic and elastic media, the equation 2.1.17 can still be used. Disregarding external forces and assuming a propagating wave with angular frequency ω

$$\mathbf{u}(\mathbf{x}, t) = \mathbf{u}(\mathbf{x})e^{-i\omega t} \tag{2.2.1}$$

so,

$$\mu\nabla^2\mathbf{u}(\mathbf{x}) + (\lambda + \mu)\nabla(\nabla \cdot \mathbf{u}(\mathbf{x})) = -\rho\omega^2\mathbf{u}(\mathbf{x}) \tag{2.2.2}$$

The above equation describes the wave propagation. However, boundary conditions are needed in order to obtain a complete set of solutions. These conditions are obtained by analyzing the fluid-solid interface and by imposing the Sommerfeld radiation condition faraway from the borehole axis, as discussed bellow.

2.2.1 Solid

The solution of equation 2.2.2 can be obtained by separating the displacement field into one compressional and two polarized shear components

$$\mathbf{u}(\mathbf{x}) = \mathbf{u}^P(\mathbf{x}) + \mathbf{u}^{SH}(\mathbf{x}) + \mathbf{u}^{SV}(\mathbf{x}) \tag{2.2.3}$$

here $\mathbf{u}^P$ denotes the compressional displacement, $\mathbf{u}^{SH}$ is the horizontally polarized shear component, and $\mathbf{u}^{SV}$ is the vertically polarized shear components. Using the cylindrical coordinate system (with $\mathbf{u} = (u_r, u_\theta, u_z)$), the displacement potentials (Φ, χ, Γ) can be introduced in a convenient way [27]

$$\begin{aligned} \mathbf{u}^P &= \nabla\Phi \\ \mathbf{u}^{SH} &= \nabla \times (\chi\hat{\mathbf{z}}) \\ \mathbf{u}^{SV} &= \nabla \times \nabla \times (\Gamma\hat{\mathbf{z}}) \end{aligned} \tag{2.2.4}$$

and, then, each potential has to satisfy its Helmholtz equation

$$\begin{aligned}(\nabla^2 + k_p^2)\Phi &= 0\\ (\nabla^2 + k_s^2)\chi &= 0\\ (\nabla^2 + k_s^2)\Gamma &= 0\end{aligned} \tag{2.2.5}$$

where the compressional and shear wavenumbers are given by $k_p = \omega/v_p$ and $k_s = \omega/v_s$. The compressional and shear velocities are given by equation 2.1.18. Considering a planar wave propagating along the z-direction, the general solution of equation 2.2.5 is [27]

$$\begin{aligned}\Phi(r,\theta,z) &= [A_n I_n(pr) + B_n K_n(pr)]\, e^{ik_z z} \cos[n(\theta-\theta_0)]\\ \chi(r,\theta,z) &= [C_n I_n(sr) + D_n K_n(sr)]\, e^{ik_z z} \sin[n(\theta-\theta_0)]\\ \Gamma(r,\theta,z) &= [E_n I_n(sr) + F_n K_n(sr)]\, e^{ik_z z} \cos[n(\theta-\theta_0)]\end{aligned} \tag{2.2.6}$$

In the above expression, I_n is the modified Bessel function of the first kind and order n, K_n is the modified Bessel function of the second kind and order n. Moreover, the number n is interpreted as the mode number, with $n = 0$ representing the monopole mode, $n = 1$ representing the dipole mode, and so on. θ_0 is the initial phase. k_z is the propagating wavenumber in the z-direction. The parameters p and s represent the compressional and shear radial wavenumbers and are given by

$$\begin{aligned}p &= \sqrt{k_z^2 - k_p^2}\\ s &= \sqrt{k_z^2 - k_s^2}\end{aligned} \tag{2.2.7}$$

2.2.2 Fluid

The fluid can be also described by equation 2.2.2, by replacing $\mu = 0$. Since fluids do not support shear, the only potential needed is the one for compressional waves (ϕ)

$$\begin{cases}(\nabla^2 + k_f^2)\phi = 0,\\ \quad u_r^f = \nabla\phi,\end{cases} \tag{2.2.8}$$

where $k_f = \omega/v_f$ is the fluid compressional wavenumber, v_f is the compressional velocity of the fluid. The fluid displacement in $\hat{r}$ direction is labeled as u_r^f. The solution of the Helmholtz equation for compressional wave potential is similar to the previously obtained for solids:

$$\phi(r,\theta,z) = \left[A_n^{'} I_n(fr) + B_n^{'} K_n(fr)\right] e^{ikz} \cos[n(\theta-\theta_0)], \tag{2.2.9}$$

where n represents the mode number and f is the fluid compressional radial wavenumber given by:

$$f = \sqrt{k_z^2 - k_f^2} \tag{2.2.10}$$

To a full description of the wave fields, the coefficients in equations 2.2.6 and 2.2.9 are needed, so boundary conditions must be imposed on the problem.

2.2.3 Boundary conditions

Figure 2.7(a) and 2.7(b) represent the general dependence with r of the Bessel modified functions of first and second order, respectively, for a given n. As we observe, $I_n(r)$ diverges for large values of r, while $K_n(r)$ behaves the same way when $r \to 0$. The source is located inside the borehole and we can use the Sommerfeld radiation conditions. This means that, in order obtain finite acoustic fields in the fluid domain ($0 \leq r \leq R$), we need to set $B_n^{'} = 0$ in equation 2.2.9. For the solid domain ($R \leq r \leq \infty$), the same argument leads us to to set $A_n = C_n = E_n = 0$ in equation 2.2.6.

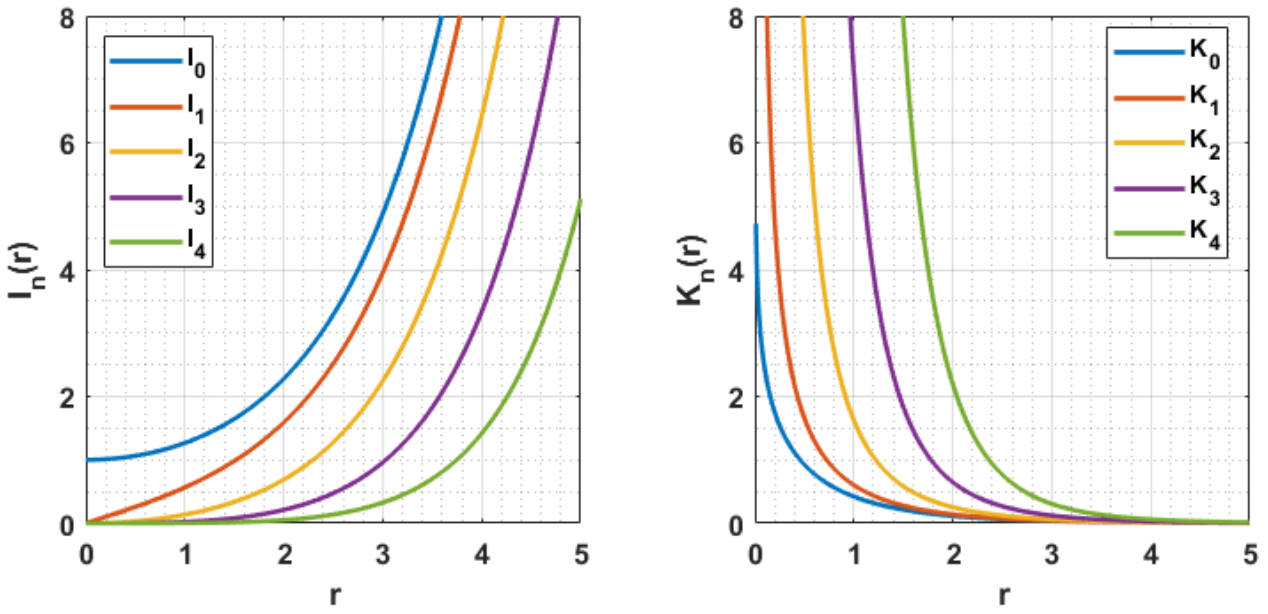

(a) (b)

Figure 2.7: Modified Bessel of (a) first and (b) second kind of order 0,1,2,3 and 4. The coordinate r is in arbitrary units.

Then, the following equations can properly describe the system:

$$\begin{cases} \phi(r,\theta,z) = A_n^{'} I_n(fr) e^{ik_z z} \cos\left[n\left(\theta - \theta_0\right)\right] & 0 \leq r \leq R \\ \Phi(r,\theta,z) = B_n K_n(pr) e^{ik_z z} \cos\left[n\left(\theta - \theta_0\right)\right] & R \leq r \leq \infty \\ \chi(r,\theta,z) = D_n K_n(sr) e^{ik_z z} \sin\left[n\left(\theta - \theta_0\right)\right] & R \leq r \leq \infty \\ \Gamma(r,\theta,z) = F_n K_n(sr) e^{ik_z z} \cos\left[n\left(\theta - \theta_0\right)\right] & R \leq r \leq \infty \end{cases} \tag{2.2.11}$$

To be able to solve the system of equations (2.2.11), another four boundary conditions are required. These conditions can be obtained by analyzing the borehole interface ($r = R$). The radial displacement u_r and radial stress σ_{rr} must be continuous and, since the fluid doesn't support shear, the shear stresses σ_{rz} and $\sigma_{r\theta}$ must vanish at the interface. These conditions can be expressed as follows:

$$\begin{cases} u_r = u_r^f \\ \sigma_{rr} = \sigma_{rr}^f \\ \sigma_{rz} = 0 \\ \sigma_{r\theta} = 0 \end{cases} \qquad r = R. \tag{2.2.12}$$

Using equations 2.1.3, 2.1.7, and 2.1.13, the stress elements in cylindrical coordinates are given by

$$\sigma_{ij} = \lambda(e_{rr} + e_{\theta\theta} + e_{zz})\delta_{ij} + 2\mu e_{ij} \tag{2.2.13}$$

where the strain components are given by:

$$\begin{aligned} e_{rr} &= \frac{\partial u_r}{\partial r} \\ e_{\theta\theta} &= \frac{u_r}{r} + \frac{1}{r}\frac{\partial u_\theta}{\partial \theta} \\ e_{zz} &= \frac{\partial u_z}{\partial z} \\ e_{r\theta} &= \frac{1}{2}\left[\frac{1}{r}\frac{\partial u_r}{\partial \theta} - \frac{u_\theta}{r} + \frac{\partial u_\theta}{\partial r}\right] \\ e_{\theta z} &= \frac{1}{2}\left[\frac{1}{r}\frac{\partial u_z}{\partial \theta} + \frac{\partial u_\theta}{\partial z}\right] \\ e_{rz} &= \frac{1}{2}\left[\frac{\partial u_z}{\partial \theta} + \frac{\partial u_r}{\partial z}\right] \end{aligned}$$

and the displacement components can be expressed using equations 2.2.11

$$\begin{aligned} u_r &= \frac{\partial \Phi}{\partial r} + \frac{1}{r}\frac{\partial \chi}{\partial \theta} + \frac{\partial^2 \Gamma}{\partial r \partial z} \\ u_\theta &= \frac{1}{r}\frac{\partial \Phi}{\partial r} + \frac{\partial \chi}{\partial \theta} + \frac{\partial^2 \Gamma}{\partial r \partial z} \\ u_z &= \frac{\partial \Phi}{\partial z} + k_s^2 \Gamma + \frac{\partial^2 \Gamma}{\partial z^2} \end{aligned}$$

The above equations applied to the boundary conditions 2.2.12 lead to a homogeneous system of the form [8]:

$$\begin{pmatrix} H_{11} & H_{12} & H_{13} & H_{14} \\ H_{21} & H_{22} & H_{23} & H_{24} \\ H_{31} & H_{32} & H_{33} & H_{34} \\ H_{41} & H_{42} & H_{43} & H_{44} \end{pmatrix} \begin{pmatrix} A'_n \\ B_n \\ D_n \\ F_n \end{pmatrix} = \begin{pmatrix} 0 \\ 0 \\ 0 \\ 0 \end{pmatrix} \tag{2.2.14}$$

where

$$\begin{aligned}
H_{11} &= -\frac{nI_n(fR)}{R} - fI_{n+1}(fR) \\
H_{21} &= \rho_f \omega^2 I_n(fR) \\
H_{31} &= H_{41} = 0 \\
H_{12} &= \frac{nK_n(pR)}{R} - pK_{n+1}(pR) \\
H_{22} &= \frac{2\rho v_s^2 n(n-1)K_n(pR)}{R^2} + \rho(2k_z^2 v_s^2 - \omega^2)K_n(pR) + \frac{2\rho p v_s^2 K_{n+1}(pR)}{R} \\
H_{32} &= \frac{2n\rho v_s^2}{R}\left[pK_{n+1}(pR) - \frac{(n-1)K_n(pR)}{R}\right] \\
H_{42} &= 2ik_z\rho v_s^2\left[\frac{nK_n(pR)}{R} - pK_{n+1}(pR)\right] \\
H_{13} &= \frac{nK_n(sR)}{R} \\
H_{23} &= \frac{2\rho v_s^2 n(n-1)K_n(sR)}{R^2} - \frac{2n\rho s v_s^2 K_{n+1}(sR)}{R} \\
H_{33} &= -\rho v_s^2\left\{\left[s^2 + \frac{2n(n-1)}{R^2}\right]K_n(sR) + \frac{2sK_{n+1}(sR)}{R}\right\} \\
H_{43} &= \frac{ik_z n\rho v_s^2 K_n(sR)}{R} \\
H_{14} &= \frac{ik_z nK_n(sR)}{R} - ik_z sK_{n+1}(sR) \\
H_{24} &= 2ik_z\rho v_s^2\left[\frac{n(n-1)}{R^2} + s^2\right]K_n(sR) + \frac{2ik_z s\rho v_s^2 K_{n+1}(sR)}{R} \\
H_{34} &= 2ik_z n\rho v_s^2\left[\frac{sK_{n+1}(sR)}{R} - \frac{(n-1)K_n(sR)}{R^2}\right] \\
H_{44} &= (k_z^2 + s^2)\rho v_s^2\left[sK_{n+1}(sR) - \frac{nK_n(sR)}{R}\right]
\end{aligned}$$

For equation 2.2.14 to have a nontrivial solution, the determinant of the matrix of coefficients must vanish. The zeros of this determinant results in the relation of the phase velocity of the guided waves. This means that for each considered angular frequency ω, one needs to find the wavenumber k_z which vanishes the determinant. Replacing $n = 0$ in the previous equations, the results obtained of Biot for Stoneley wave are recovered. [8]

The analytical solution for simple systems can be found with the formalism described above. However, the description of more complex and realistic structures are usually needed. In realistic systems, analytical solutions cannot be easily found. Numerical methods have been used in such cases. More sophisticated and accurate numerical methods to capture the physical situation have been required since the modeling plays an important role in the refinement of inversion techniques. Finite-difference time-domain (FDTD) is the most commonly used technique. We note the contributions of Cheng *et al.* [28] who numerically studied the wave propagation in isotropic and anisotropic formations; Liu *et al.* [29] who obtained synthetic waveforms for inhomogeneous solid formations. Wang and Tang [15] investigated the dipole and quadrupole sources, they also applied a perfect-matched layer (PML) to simulate infinite domains; Sinha *et al.* [30] studied transversely isotropic formations and they also applied the PML. Synthetic waveforms were obtained by Whyte and Zechman considering a cylindrical and homogeneous borehole [31]. The monopole and dipole sources in a transversely isotropic solid were studied by Tongtaow [32]. The theoretical formulation and numerical evaluation of the axisymmetric and non-axially symmetric mode of higher-order in a fluid-filled borehole surrounded by a homogeneous medium were developed by Kurkjian and Chang [10]. Cheng and Tokzos theoretically formulated and numerically evaluated the dispersion curve and synthetic microseismograms for Stoneley waves considering an elastic tool [33].

More recently, the FEM has been employed to simulate acoustic sonic logging and wave propagation phenomena in geometrically complex situations. Pardo *et al.* [18, 19] obtained the waveforms and the dispersion curves of the propagating modes in wireline and logging-while-drilling techniques with an eccentred tool. Matuszyk, Torres-Verdín and Pardo [20] and Matuszyk and Torres-Verdín [21] numerically studied different and complex geometric configurations in logging-while-drilling and wireline situations: the presence of the tool (with and without grooves), fractures, and layering. They explored the axial symmetry of the system and implemented a 2D model in which formation non-uniformities in the radial and axial directions are easily tailored. They also applied a PML to mimic the infinite formation and introduced an adaptative mesh formulation which increased the numerical accuracy of the results. Gaede *et al.* [34] studied the dynamic properties in 3D vertical and inclined boreholes in a variety of situations including in isotropic, transversely isotropic, and orthorhombic symmetries. Jorgensen and Burns [16] studied the response of a stressed acoustic borehole excited by a quadrupole source and

computed its dispersion curves. In the next chapter, we use FEM calculations in order to obtain the dispersion curves for each propagating mode of the borehole. The considered modes are solutions for equation 2.2.14 using $n = 0, 1, 2$, that represent the Stoneley, flexural, and screw mode, respectively.

Chapter 3

Modal Analysis

In this chapter, we investigate the acoustic modes and their dispersion curves in infinite, isotropic, and homogeneous formations in the frequency domain. We describe and validate our implementation by comparing our numerical results with the analytical solutions obtained in Chapter 2. Moreover, the main result obtained by Biot [9] about the Stoneley wave is reproduced and then expanded for flexural waves. Finally, we discuss the main aspects of each propagating mode.

3.1 Model implementation

The numerical simulation was performed using the FEM with COMSOL *Multiphysics*. It provides a useful and friendly platform that allows us to solve Partial Differential Equations (PDEs) in different physical environments (like liquids and solids) and to couple them via appropriate boundary conditions. It counts with some already implemented PDEs for different purposes, like the constitutive equations of the elasticity theory described in Chapter 2.

Our simulations use *Solid Mechanics* and *Pressure Acoustics* packages. The first one is applied to the solid domain and the second to the fluid domain. At the borehole interface, the coupling uses the *Acoustic-Structure Boundary*. It allows us to numerically solve the elastodynamic equation in the considered medium (equation 2.1.17), as developed in Chapter 2. To directly obtain the propagating modes, we used the *Modal Analysis* study type. The modal analysis is a study in the frequency-domain focused on finding normal modes of the considered structure, meaning the eigenvalue of the stiffness matrix.

In our simulation, the modal analysis consists in considering a propagating plane-wave along the z-axis with wavenumber k_z. The problem can be solved just considering the xy plane, simplifying from 3D to 2D calculations. In this way, the solid displacement vector

and fluid acoustic pressure can be described by the following transformations

$$\begin{aligned} \mathbf{u}(x,y,z) &= \mathbf{u}(x,y)e^{-ik_z z} \\ p(x,y,z) &= p(x,y)e^{-ik_z z} \end{aligned} \tag{3.1.1}$$

The above considerations, together with the symmetry of the problem, lead to some reductions in the computational domain. Basically, for each frequency f, values for k_z will be searched to solve the governing equations with imposed boundary conditions. Strictly speaking, the wavenumber is composed of an imaginary and a real part

$$k_z = k_z^{real} + ik_z^{imag} \tag{3.1.2}$$

A propagating mode happens when $k_z^{imag} = 0$. A evanescent wave is described by a purely imaginary wavenumber ($k_z^{real} = 0$). When both are different from zero, meaning complex values of k_z, we have a mode that is attenuated along the propagation path, so-called leaky mode. In this work, we have only considered the real part of the wavenumber, disregarding the attenuation of the wave. Then, the search routine is based on finding purely real values of k_z.

Figure 3.1(a) illustrates the infinite borehole aligned along the z-axis. A cut plane used to investigate the modes is indicated. Figure 3.1(b) shows the cut plane which is implemented in COMSOL in details. The light brown and blue regions indicate the solid and fluid domains. The fluid-solid interface boundary conditions (red dashed line) are given by equation 2.2.12.

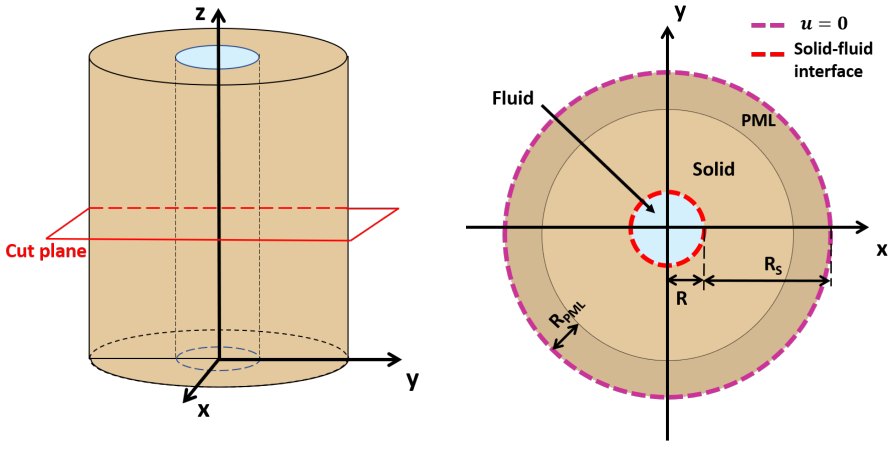

(a) (b)

Figure 3.1: Computational domains used to investigate the propagating modes: (a) shows the 3D domain and the cut plane considered that simplifies the considered problem; (b) 2D sketch of the implemented modal analysis model showing the liquid and solid domains as well as their interface. R is the fluid radius, R_{PML} is the PML width, R_s is the cylindrical shell width. $\mathbf{u} = 0$ represents zero displacement at the model outer edge.

Figure 3.1(b) also shows the presence of PML layer. The PML is an artificial layer used to mimic infinite domains which is commonly used in frequency-domain studies for wave-like equations. It is a mapping of the real coordinates into complex ones, providing the attenuation of incoming waves. The PML outer boundary ($\mathbf{u} = 0$) helps to guarantee the attenuation of the modes at the model edge. The layer needs to have the same meshing parameters of the adjacent domain and the coordinates transformation parameters have to be carefully chosen to avoid reflections and unexpected interactions. The stretching in one single direction is given by the transformation

$$\Delta x = \lambda b \xi^a (1 - i) - \Delta_w \xi \tag{3.1.3}$$

where λ is the typical wavelength of incoming waves; $\Delta_w = x_1 - x_0 = R_{PML}$; a and b are the curvature and scaling parameters, respectively. ξ is a parameter considered for each point x inside the PML domain, it varies from 0 to 1 and is given by:

$$\xi = (x - x0)/(\Delta_w) \tag{3.1.4}$$

Curvature and scaling parameters usually need to be optimized and can be crucial in certain systems. In our simulation, due to the domain sizes and propagating wavelengths of interest, they are not critical. For simulations shown here, we use $a = 3$ and $b = 4$. The total displacement is computed summing up the stretching for x and y directions [35, 36]. The geometric parameters used in the simulations presented here are given in Table 3.1.

Table 3.1: Parameters used in modal simulations, considering the cut plane, as shown in Figure 3.1.

Domain	Inner radius (m)	Outer radius (m)
Fluid	0	0.1
Formation	0.1	0.8
PML	0.8	1.0

The mesh size is a key parameter to the numerical accuracy of the FEM method. Each mesh element needs to be small enough in comparison to the propagating wavelength to guarantee good resolution and accuracy of computed physical quantities. In a frequency study type, a meshing procedure can be adapted to each frequency of the sweeping. This allows us to reduce the total computational effort and maintain simulation accuracy. For each frequency, the maximum element size h is chosen to be at least ten times smaller

than the typical wavelength

$$h = \frac{v_{min}}{10\, f}, \tag{3.1.5}$$

where f is the frequency and v_{min} is the smallest mode velocity of the domain. For solids, the smallest velocity is the shear wave velocity.

The solid and fluid domains are meshed with triangular elements that are structured to guarantee the accuracy at the fluid-solid interface. Second-order shape functions in all domains were used. The PML mesh is also constructed using structured meshes composed of at least eight layers, as recommended by COMSOL *Multiphysics* User's Guide [36]. Figure 3.2(a) shows the resulting discretization map obtained at 8 kHz of a fast formation using the conditions described above. We plot one-quarter of the model geometry. The color scale presents the mesh element size distribution. Figure 3.2(b) is a zoom in the fluid-solid interface, demonstrating the mesh parameterization according to the fluid or solid velocities, as well as the mesh resolution at the fluid-solid interface.

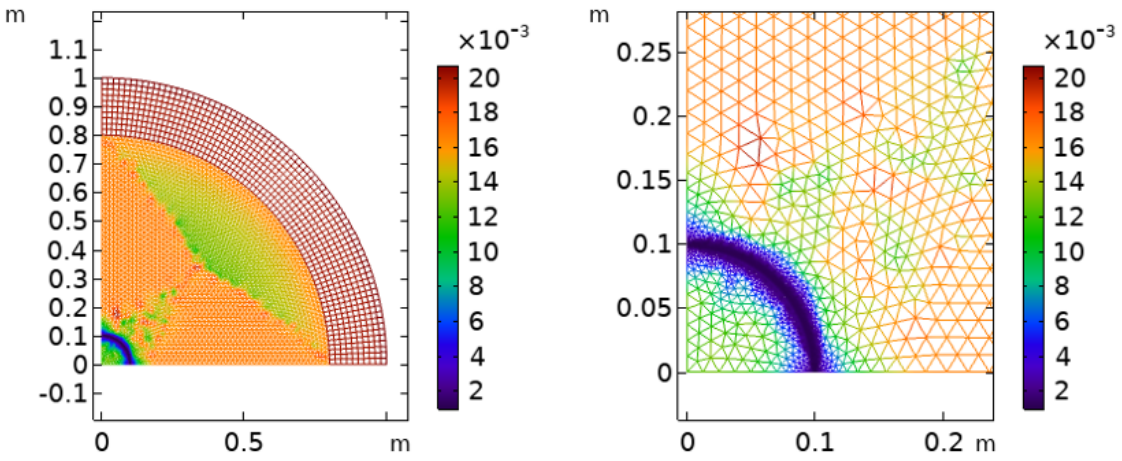

(a) (b)

Figure 3.2: (a) Discretization of the domain. (b) Zoom near to solid-fluid interface. Color scale shows the mesh element size.

3.2 Results

Our main goal is to calculate the dispersion curves for the propagating modes in fast and slow formations. The dispersion curve is commonly represented by a chart of the angular frequency as a function of the wavenumber. However, in geophysics, dispersion curves are commonly represented as the inverse of phase velocity v_{phase}, known as phase slowness S, in the function of frequency. The slowness is given by

$$S = \frac{K}{v_{phase}} \tag{3.2.1}$$

where $K = 304800$ is the conversion factor from s/m to µs/ft, which is the most used unit in sonic well logging.

In order to validate and test our implementation, we choose parameters for fluid and solid domain which are typical in numerical studies [8, 32, 37], providing a straightforward comparison between the results. We point out that changes in elastic parameters of each medium can be easily implemented in our platform. Fast and slow formations were simulated using different values for fluid compressional slowness. The chosen slowness are displayed in Table 3.2. Fluid 1 was used for fast formation calculation since its slowness is greater than solid shear slowness. Fluid 2 was used for slow formation calculation since its slowness is lower than solid shear slowness.

Table 3.2: Parameters used for simulation of fast and slow formations. Fast formation considers the fluid 1, whereas slow formation considers fluid 2.

Domain	S_p (µs/ft)	S_s (µs/ft)	ρ (kg/m^3)
Fluid 1	203.0	-	1000
Fluid 2	138.5	-	1000
Formation	87.0	152.4	2300
PML	87.0	152.4	2300

Figures 3.3(a) and 3.3(b) summarize (in open circles) the results of our FEM simulations for fast and slow formations, respectively. The upper (high slowness) slightly dispersive mode corresponds to the Stoneley wave. The highly dispersive mode which shows a slowness plateau ($S \approx 152$ µs/ft) as frequency becomes smaller than 3 kHz is associated with the flexural mode. The second highly dispersive mode which shows the plateau for frequencies below 6 kHz is the quadrupole (screw) mode [38]. More details about these modes will be discussed in Section 3.3. One can also note the presence of higher-order modes in Figure 3.3(a). The dispersive character of these modes starts at much higher frequencies and we are not interested in their behavior since they are not used in real logging situations. We note, however, that calculations at higher frequencies reveal a similar behavior, in terms of curve shape, to lower-order modes. FEM calculation also provides desired information about modes in the low-frequency range.

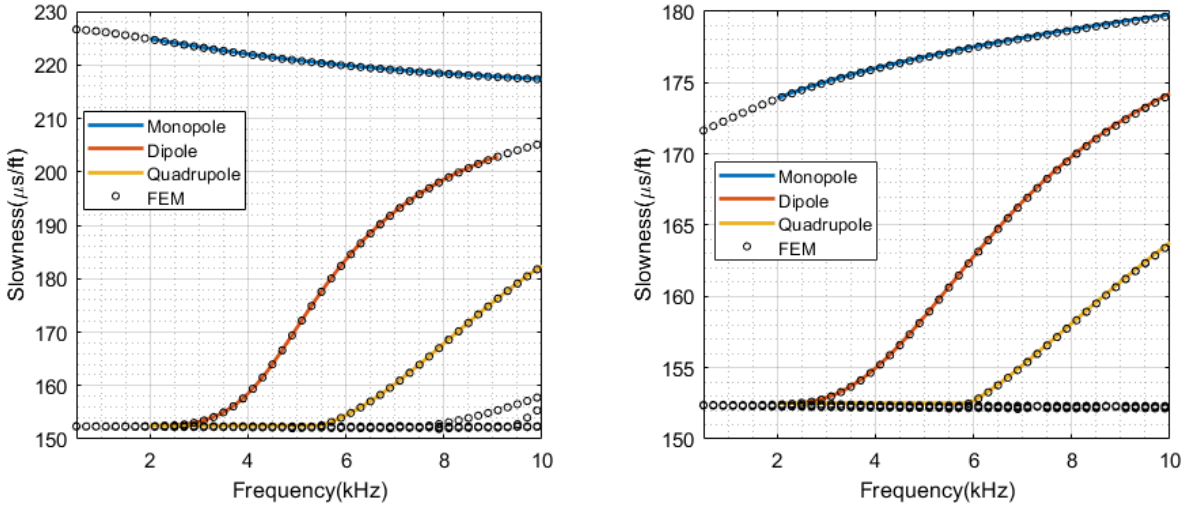

Figure 3.3: Dispersion relation of the monopole, dipole, and quadrupole modes obtained by FEM, in open circles, for (a) Fast formation and (b) Slow formation. The numerical solution of Equation 2.2.14 for $n = 0$, 1, and 2 corresponding to the Stoneley (monopole), flexural (dipole), and quadrupole modes are plotted for comparison.

In order to validate our simulation, we compared our results with a numerical solution of Equation 2.2.14 [1]. This approach consists in numerically finding the elements H_{mn} depend on n, ω and k_z using the parameters we presented in Tables 3.1 and 3.2. For n = 0, 1, and 2 we have the solutions for the Stoneley, flexural, and quadrupole modes, respectively. The imposition of $Det(H) = 0$, meaning non-trivial solutions, for each chosen mode, provides its dispersion curves. Thus, the method consists of finding values for k_z and ω that vanish the determinant of the modal matrix. The implementation needs to handle with modified Bessel functions with complex values. The elements depend on the radial wavenumbers given by equations 2.2.7 and 2.2.10. Thus, when $k_z < \omega/v_i$ ($v_i = v_f, v_s, v_p$), the radial wavenumbers s, p, f assume complex values, implying leaky modes. The implemented algorithm does not deal with this situation. According to the literature, the flat region at low frequencies, found in our calculations, is related to the leaky character of the mode. In this frequency region, there is a loss of energy to the formation. [39]

Figure 3.3 also shows the comparison between FEM simulation and the ones obtained by the method based on the modal matrix. As we observe, the results are in very good agreement for monopole, dipole, and quadrupole modes in the whole range of frequencies from 2 kHz to 10 kHz. Moreover, FEM simulation can successfully describe dipole and quadrupole behavior in the low-frequency limit and, when the frequency tends to zero, we obtain the slowness shear wave velocity of the surrounding medium, as expected from

[1] implemented by Dr. Pablo D. Batista

Table 3.2. Using the meshing parameters described in the previous section and the geometrical values presented in Table 3.1, our FEM model is able to calculate accurately the dispersion curves up to 200 Hz, which is one order of magnitude smaller than what is usually detected with reasonable signal-to-noise ratios in sonic logging experiments [8].

We can also use our FEM simulation to investigate the spatial distribution and symmetry of each mode. Figure 3.4 shows the solid total displacement (in meters) and fluid acoustic pressure (in Pascal) at 8 kHz. We can observe that the acoustic pressure is lower at the borehole center and greater near to the borehole wall, demonstrating the guided nature of the Stoneley (Figure 3.4(a)), flexural (Figures 3.4(c) and 3.4(d)), and quadrupole (Figure 3.4(b)) modes. The figure also reveals how the coupling between the fluid and the rock occurs for each mode. One can observe that Stoneley mode ($n = 0$) is totally symmetric, as expected. The flexural mode ($n = 1$) presents a preferential direction, and two possible orientations can be seen. The quadrupole mode ($n = 2$) exhibits two preferred directions and two possible orientations, one of them is plotted.

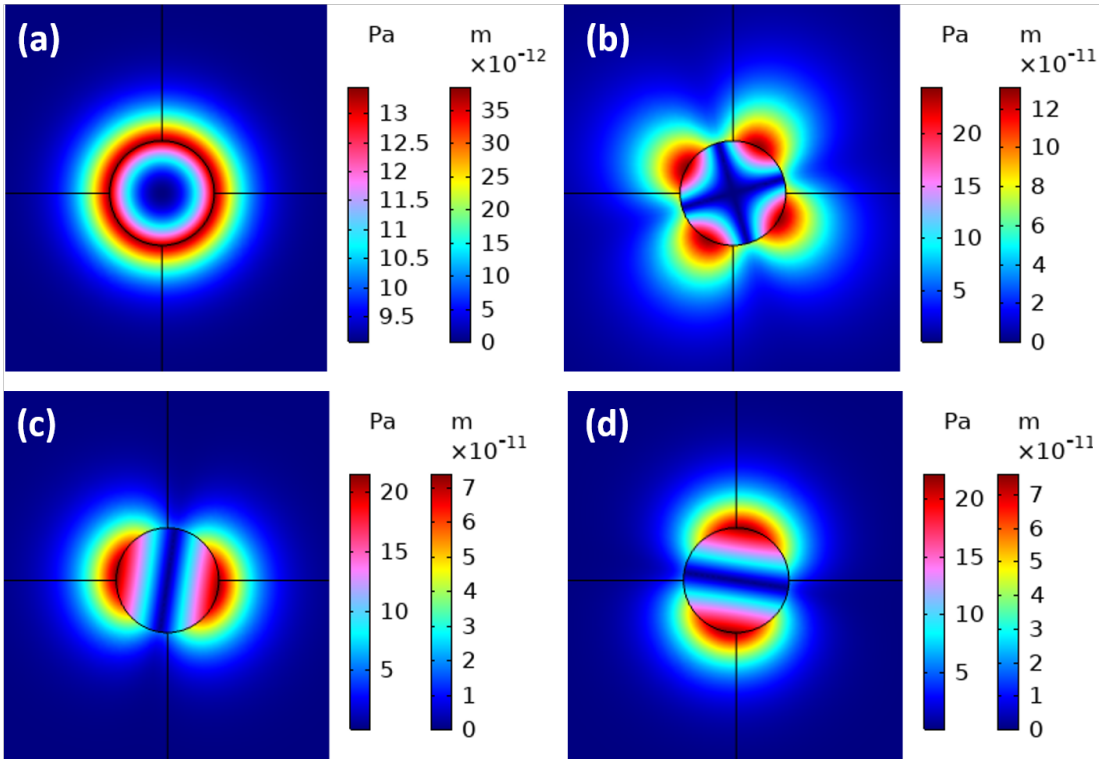

Figure 3.4: Visualization of the modes and the coupling between the fluid and the solid at 8 kHz . The pressure is given in Pa, and the radial displacement is given in m. The represented modes are: (a) Stoneley mode (b) Quadrupole mode (c) and (d) two different Flexural mode.

To reduce the computational efforts, the simulated domain size can be diminished even more using cyclic boundary condition, as shown in Figure 3.5(a). This boundary condition is based on the choice of the azimuthal mode number n, which is the same who labeled the monopole, dipole, and quadrupole modes. The mode number available in this

configuration varies from 0 to $N/2$, where N is the number of necessary sectors to a full revolution. To our interests, it is just needed to use one-quarter of the total circle as shown in Figure 3.5(a).

The validation of this implementation can be done comparing the obtained results with the previous ones, as shown in Figure 3.5(b). In open circles we reproduce the results shown in Figure 3.3(a) for the fast formation. In colored solid lines, we show the results obtained by the reduced model shown in Figure 3.5(a). Both computed curves are in total agreement. Therefore, the domain with a periodic condition can be used henceforward.

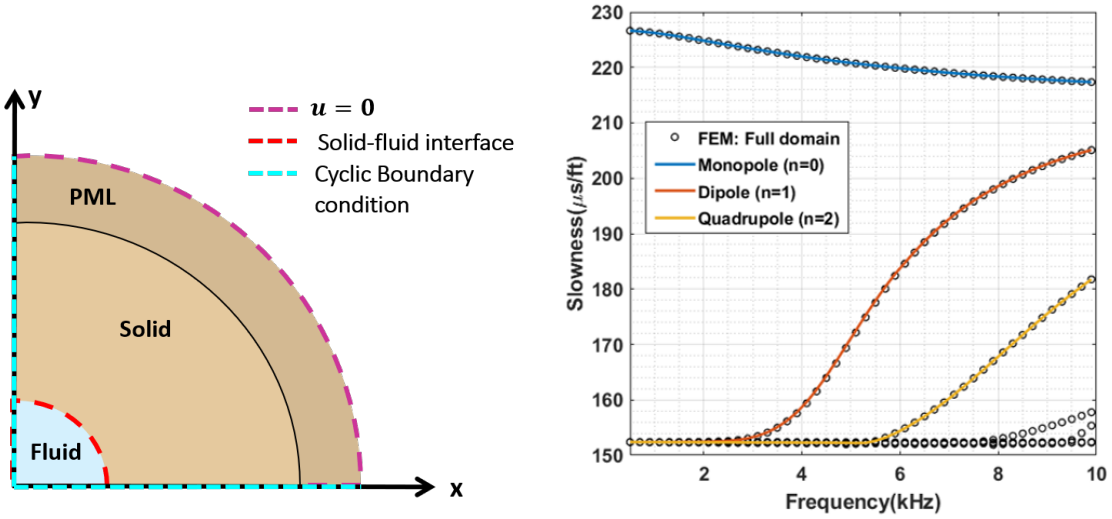

(a) (b)

Figure 3.5: (a) Geometry used to reduce the computational domain size using boundary conditions. The sector angle is $\pi/4$. The solid domain, fluid domain, and the PML layer are represented. (b) Comparison between the dispersion curves using the full domain resented in Figure 3.3(a) and the reduced domain in the fast formation.

In order to further test our implementation, we reproduce the first analytical (and fundamental) result demonstrated by Biot in 1952 for the propagation of Stoneley modes [9]. Biot analytically studied the Stoneley mode and obtained fundamental relations fundamental between the fluid and rock elastic parameters of this mode. The problem was analyzed for different values of the ratio between fluid and solid densities $\rho_f/\rho = 0.4, 0.6, 0.8, 1.0$ in order to observe the influence of the fluid properties in the dispersion curve. To numerically reproduce his work, the formation parameters are given in Table 3.3 were used. The geometrical parameters are the same from Table 3.1.

Table 3.3: Parameters used in simulations to reproduce the results in reference [9].

Domain	S_p (µs/ft)	S_s (µs/ft)	ρ (kg/m^3)
Fluid 1	203.0	-	920
Formation	78.2	135.5	2300
PML	78.2	135.5	2300

Figure 3.6(a) shows the normalized dispersion curves obtained by FEM for the Stoneley mode using the same density ratios computed by Biot. Instead of the slowness, we plot the phase velocity in order to make a direct comparison between our simulations and his results. The formation phase velocity (v_{phase}) is normalized with respect to the fluid velocity (v_f) and is plotted as function of $\lambda/2R$, where $\lambda = v_{phase}/f$. Our numerical results are in extremely good agreement with Biot analytical ones (see. Figure 8 from [9]). The velocity tends to an asymptotic value in the low frequency limit, as indicated in Figure 3.6(a). The asymptotic value that was derived by Biot is given by:

$$\frac{v_{phase}}{v_f} = \frac{1}{\sqrt{1 + (\rho_f v_f^2/\rho v_s^2)}} \tag{3.2.2}$$

The asymptotic values are organized in Table 3.4, where the predicted values using equation 3.2.2 are compared to the ones obtained with our simulations. Independent of the density ratio, the difference between the two results is not larger than 1.6%.

Table 3.4: Analytical and numerical comparison between the ratio of the Stoneley phase velocity and fluid velocity for different fluid density ratios in the low-frequency limit.

Densities ratio ρ_f/ρ	**Theoretical value** v_{phase}/v_f	**FEM** v_{phase}/v_f
0.4	0.921	0.922
0.6	0.888	0.887
0.8	0.858	0.864
1.0	0.832	0.845

The same analysis can be done for the flexural mode. This is presented in Figure 3.6(b). Again, the mode is much more dispersive than the Stoneley. As expected, for high wavelength (low frequencies) the phase velocity tends to shear wave formation [8], as observed by comparing the values displayed in Table 3.3. By analyzing the low frequency limit, the value of the phase velocity is $v_{phase} = 1.5v_f = 2252.2$ m/s, in terms of the phase slowness $S \approx 135$ µs/ft.

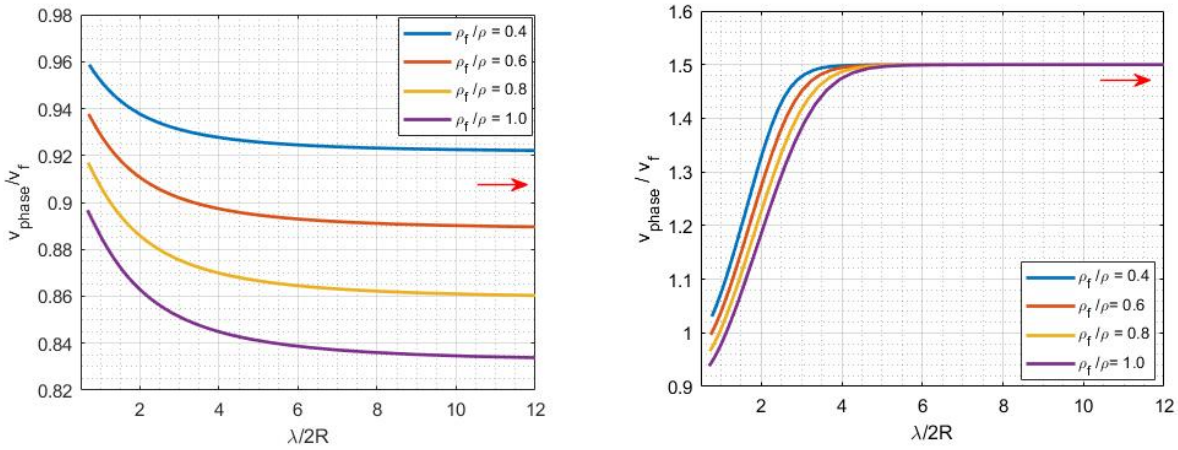

(a) (b)

Figure 3.6: Normalized formation phase velocity as a function of normalized wavenumber in fast formation for: (a) Stoneley and (b) Flexural modes. Different values of fluid and solid density ratios are considered: $\rho_f/\rho = 0.4, 0.6, 0.8, 1.0$. The red arrow indicates the low-frequency limit.

3.3 Physical interpretation of the modes

The analysis of dispersion curves gives us information about the surrounding medium. In general, field detected acoustic data is numerically processed (some of the methods are discussed in the next chapter) to generate the dispersion curves of the formation as a function of the borehole depth [1]. However, the elastic properties of real rocks vary considerably with stress, porosity, and composition. This means that in a single borehole, which generally has depths of a few kilometers, the properties of the formation can vary enormously. Therefore, the understanding of the dispersion curves is important for the interpretation of the experimental results as well as for the optimization of experimental procedures and even for the development of new logging tools and sources.

The low-frequency range is a key part of the problem since the shear velocity is usually estimated using flexural and quadrupole modes. In this regime, even the signal (energy) associated with the flexural waves competes with attenuation and noise. Consequently, a better characterization of these modes in the measurable frequency range is an important part in the estimation of the shear velocity at low frequencies.

In an acoustic logging experiment, the signal is collected as an amplitude as a function of time in each detector of the logging tool. The arriving signal can be described as a superposition of the different plane waves with different phase slowness. The energy of the wave packet propagates with group slowness given by

$$S_g(\omega) = \frac{dk\,(\omega)}{d\omega} \tag{3.3.1}$$

where ω is the angular frequency, and $k(\omega)$ is the wavenumber.

Figures 3.7(a) and 3.7(b) show the dispersion curves calculated by FEM for fast and slow formations, respectively, in a range from 200 Hz to 20 kHz, using the parameters displayed in Table 3.2. They show in continuous (solid) lines the phase slowness and in dashed lines the group slowness. The Stoneley wave (blues lines), also designated as tube wave, is symmetric. Its amplitude decays rapidly from the borehole interface and it is slightly dispersive when compared to other modes. The phase and group slowness decrease for high frequencies in the fast formation and increases in slow formation. The Stoneley dispersion depends on the compressional wave slowness. However, according to Table 3.2, since the elastic parameters of the formations are the same, the difference in the dispersion behavior shown in Figures 3.7(a) and 3.7(b) is due to the fluid properties used in each simulation. In the high-frequency limit, its phase slowness tends to the Scholte wave slowness, another type of interface wave that propagates along a planar solid-fluid interface [8, 9, 38] The phase slowness of the Scholte waves are slightly greater than fluid wave slowness. This limit can be explained, due to the fact that high frequencies result in smaller wavelengths, so the cylindrical borehole is *seen* by the wave as a planar space.

The flexural and quadrupole waves exhibit stronger dispersive characters when compared to the Stoneley wave, as we see in Figure 3.7. In the low-frequency range, their phase slowness tends to the surrounding medium shear wave slowness, meaning that the influence of the fluid can be neglected. At high frequencies, their slowness tends to the Stoneley slowness, meaning a strong influence of the fluid [8, 38]. One important thing to remark is that we are dealing with isotropic formations. It means that both shear waves, known as SV and SH, have the same slowness. In other words, this is why we also see a degenerate flexural wave Figures 3.4(c) and 3.4(d). In anisotropic formations, shear wave splits into two different waves, known as qSV and qSH, and the same behavior is reflected in flexural and quadrupole modes. It means that, at low frequencies, one flexural wave tends to qSV-wave slowness, while the second to qSH-wave slowness. [13]

The flexural and quadrupole modes also exhibit a pronounced maximum value in the group slowness dispersion, which is called *Airy Phase*. It can be shown that, for longer times after excitation by a source, the amplitude of the guided modes around the Airy phase decays slower in distance ($\propto z^{-1/3}$) in comparison to the other modes ($\propto z^{-1/2}$) [40]. This means that, for detectors placed at larger distances compared to the mode wavelength, the detected response will usually be dominated by the modes with frequencies around the *Airy Phase*. This explains why, even employing flexural wave detection to study the low-frequency limit, the signal-to-noise ratio can be very poor. This is an important aspect to consider when choosing amplitudes and frequencies of source pulse in an experimental situation.

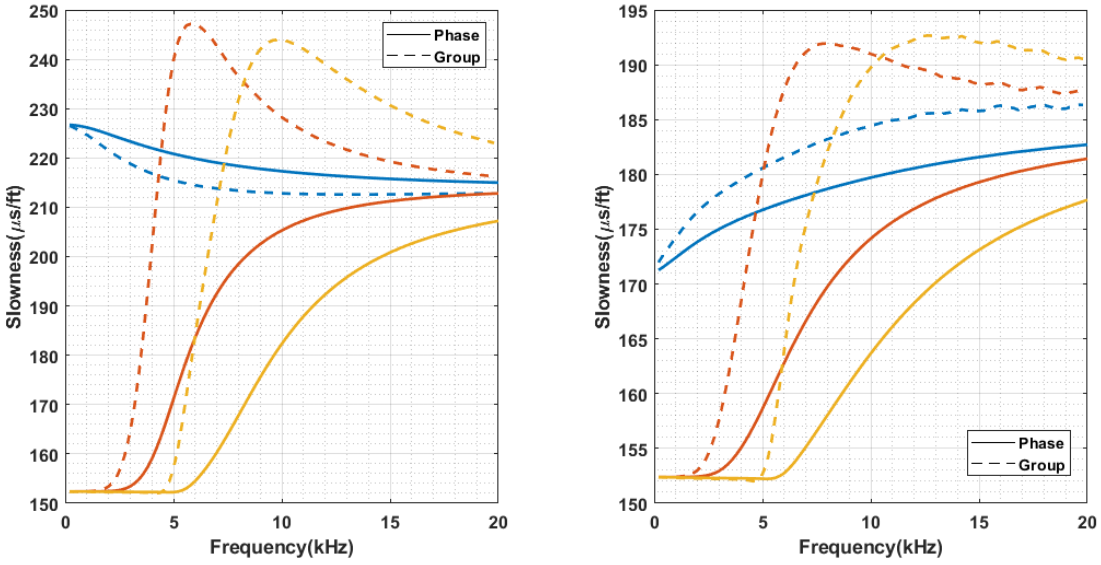

(a) (b)

Figure 3.7: Phase slowness, in a continuous line, and group slowness, in dashed line, for (a) fast and (b) slow formation. Three modes are plotted: Stoneley in blue color, flexural in orange color, and quadrupole in yellow color.

Geometric aspects of the system also affect the dispersion curve of each mode. To study these effects, dispersion curves for different borehole radius are plotted for both fast and slow formations in Figure 3.9 using the elastic parameters provided in Table 3.2. We adopted $R = 0.1, 0.2, 0.3, 0.4$ m. The phase slowness is plotted in solid lines and the group slowness is represented using a dashed line.

For the monopole mode, one can observe opposite behaviors in dispersion curves between fast and slow formations. For fast formation, Figure 3.9(a), a larger radius shifts the entire curve to left and to low slowness direction, considering a specif frequency. Whereas in slow formation, Figure 3.9(b), a larger radius shifts the curve to the left and to higher slowness values. See for example the frequency $f = 4$ kHz. In fast formation, the phase slowness is approximately 222 µs/ft for $R = 0.1$ m and 216 µs/ft for $R = 0.4$ m at this frequency. In slow formation, the phase slowness is approximately 176 µs/ft for $R = 0.1$ m and 186 µs/ft for $R = 0.4$ m at same frequency. Moreover, the phase slowness at low frequency are equal for all radii in the same type of formation, since the slowness it does not depend on geometric parameters, as calculated by Biot and is expressed by Equation 3.2.2 [9].

For dipole and quadrupole modes, the influence of the borehole radius is similar, as we observe in Figures 3.9(c) to 3.9(f). The increase of radius shifts the entire curve to left. As a result, the Airy phase is also shifted to the low-frequency range for all curves. As it is expected for these modes, the slowness phase at low-frequency range tends to the formation shear slowness independently of the borehole radius. Figures 3.9(a) to 3.9(f)

demonstrate that dispersion curve is sensitive to the borehole radius. In experiments, this geometrical parameter varies along the penetration depth. This variation, besides been much smaller in practice than the range we vary R in our simulation, adds an uncertainty in many situations. The sensitivity of the dispersion to the radius is one of the reasons why this geometrical parameter is frequently employed in fitting procedures [41].

Another way to represent the mode dispersion is to plot the normalized angular frequencies ($\omega R/v_s$) as a function of the normalized wavenumbers (kR). This type of representation is not often used in geophysics. A linear relation between ω and k represents a non-dispersive propagating wave-packet. Figures 3.8(a) and 3.8(b) show the dispersion curves of the normalized angular frequency as a function of the normalized wavenumber for the monopole, dipole, and quadrupole modes for fast and slow formations, respectively. The linear dispersion of the fluid, shear, and compressional waves are also plotted for a direct comparison. One can see that in the low-frequency limit the flexural and quadrupole modes tend to shear wave slowness (red dashed line). In the high-frequency limit, all modes tend to the Scholte wave velocity.

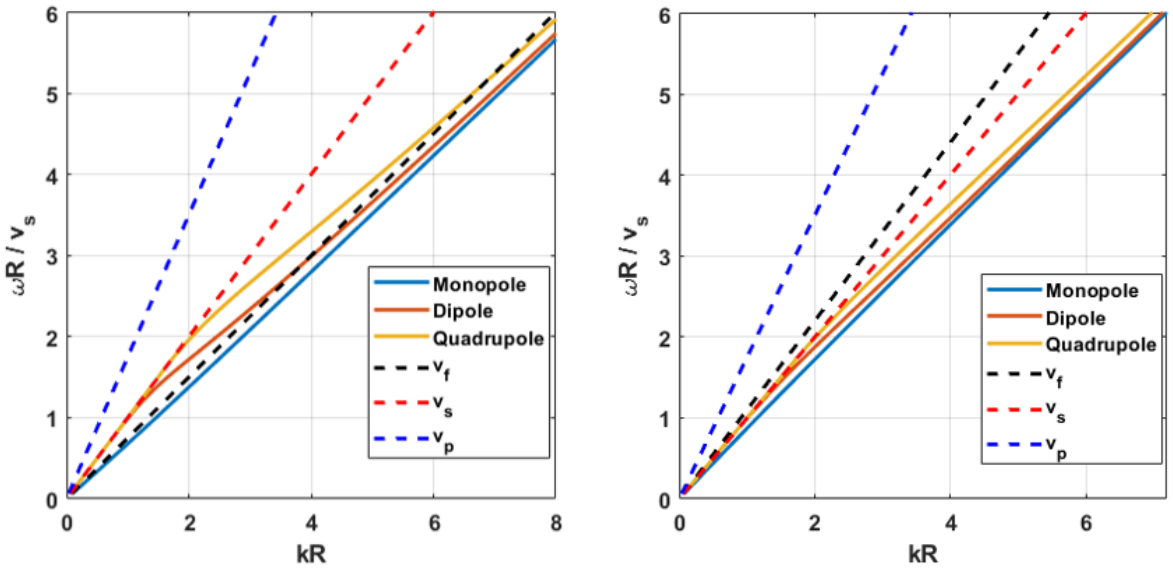

(a) Fast formation

(b) Slow formation

Figure 3.8: Dispersion relation of monopole, dipole and quadrupole modes for: (a) fast formation; (b) slow formation. The dashed blue, red and black lines represent the formation compressional, formation shear, and fluid compressional velocities, respectively.

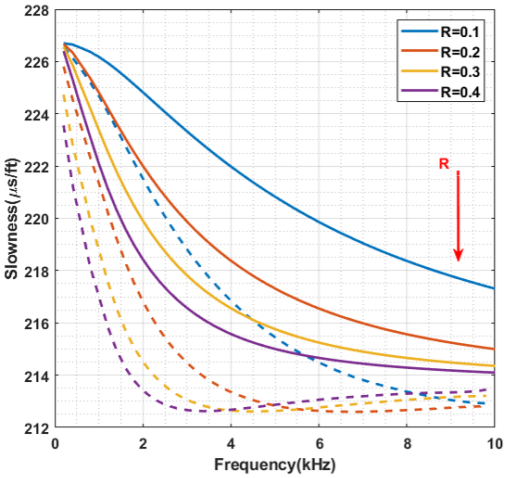

(a) Stoneley: Fast formation

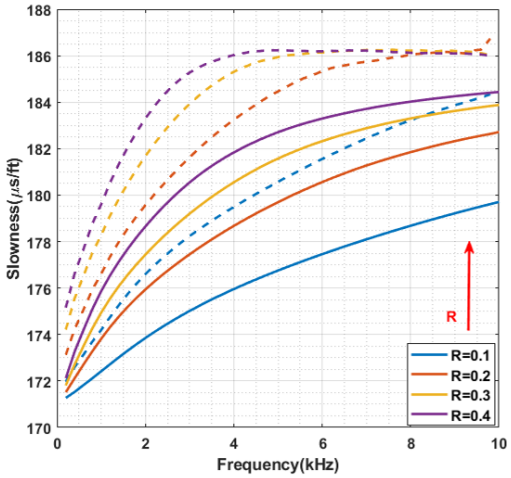

(b) Stoneley: Slow formation

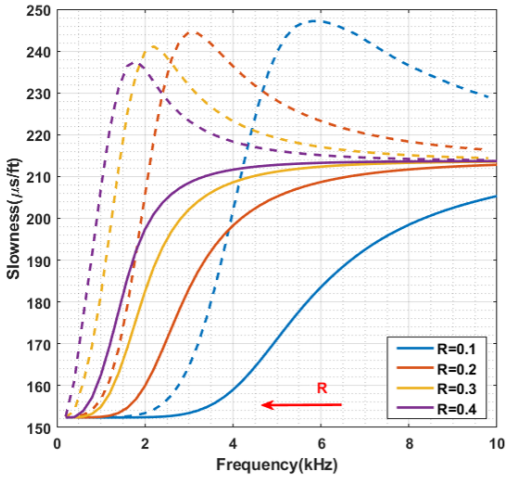

(c) Flexural: Fast formation

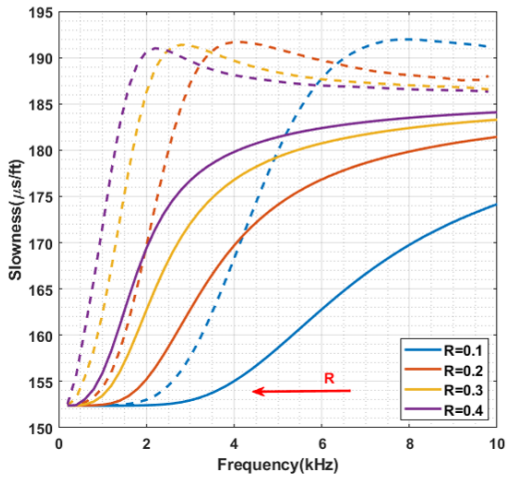

(d) Flexural: Slow formation

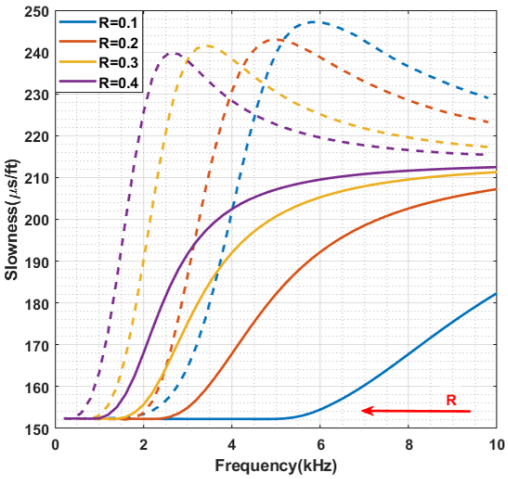

(e) Quadrupole: Fast formation

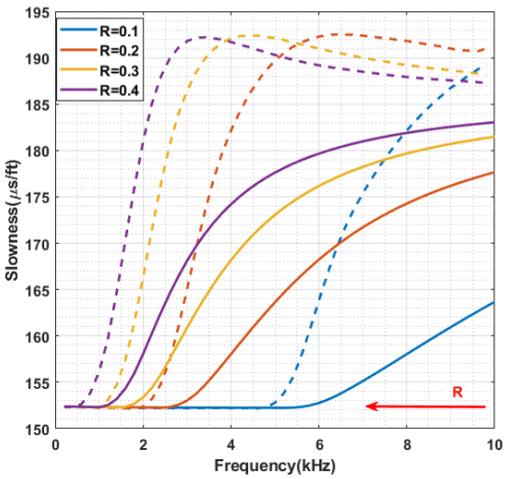

(f) Quadrupole: Slow formation

Figure 3.9: Phase slowness, in continuous line, and group slowness, in dashed line, for different radius with same elastic parameters. Stoneley mode for (a) fast and (b) slow formation. Flexural modes for (c) fast and (d) slow formation. Quadrupole modes for (e) fast and (f) slow formation. The considered radius are given in meter.

Chapter 4

Time domain analysis

In this chapter, we describe our FEM platform created to investigate fast and slow formations simulating a monopole source logging tool in an infinite, isotropic, and homogeneous formation. We obtain typical waveforms recorded in experiments, which are compared with the theory and modal analysis provided in Chapters 2 and 3.

4.1 Model implementation

Figure 4.1(a) shows the fluid-filled borehole in a 3D perspective. To obtain the solution for the axis symmetric modes like the Stoneley, the P, and the S modes, a cut plane (marked with red line) can be used to investigate the system, avoiding a 3D computation. Therefore, we solve equation 2.1.17 in the 2D plane and a full rotation around the axis of symmetry is performed afterwards. This approach has been successfully employed by Matuszyk *et al.* [20, 21] in sonic logging simulations using FEM. The general solution for the solid displacement and fluid acoustic pressure associated to the other guided modes could be obtained using the following transformation

$$\begin{aligned} \mathbf{u}(r,\theta,z,t) &= \mathbf{u}(r,z,t)e^{-in\theta} \\ p(r,\theta,z,t) &= p(r,z,t)e^{-in\theta} \end{aligned} \tag{4.1.1}$$

where n is the azimuthal number. $\mathbf{u}(r,z,t)$ and $p(r,z,t)$ are the Stoneley wave solutions, obtained by making $n = 0$. With $n = 1$ and 2 we obtain the flexural and quadrupole modes, respectively. Here, we focus our analysis on Stoneley mode.

Figure 4.1(b) shows in details the geometric aspects, boundary conditions, as well as the position of source and detectors. Wave excitation is performed by a point source emitting energy isotropically, as in the case of a monopole source. The detectors are considered as equally spaced points in which the pressure is monitored throughout time. The borehole wall (solid-fluid interface) is marked in red dashed line. To implement time-

domain simulations, we choose geometric parameters based on real experimental setups. All geometric parameters used in the simulations shown in this Chapter are organized in Table 3.1. Detectors are equally spaced by $d = 0.12$ m along the z direction and positioned at $r = 0.08$ m away from the axis of symmetry of the system.

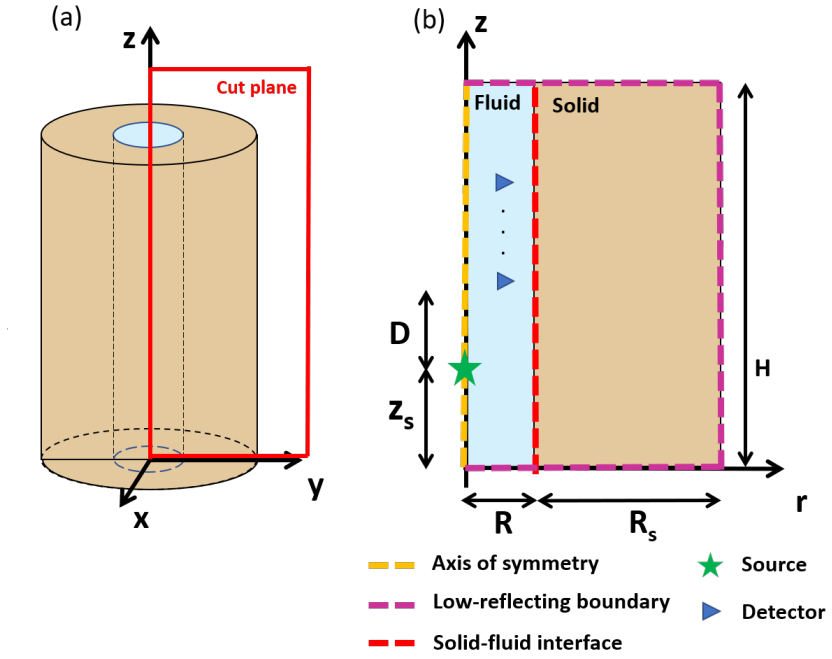

Figure 4.1: Physical and computational domains. (a) shows the fluid-filled borehole situation in a 3D perspective. It is also possible to see the presence of a cut plane, where FEM calculation takes place. (b) Shows in details geometric parameters, boundary conditions, and the positioning of source and array of detectors. In our simulations detectors are simulated by equally spaced probe points. We adopted equally spaced 10 detectors during calculations.

Table 4.1: Geometric parameters used in the tool model represented in Figure 4.1

Parameter	Value (m)
R	0.1
R_s	3
H	10
Z_s	10
D	3.5
d	0.12

The PML layer is broadly used in simulations involving frequency domain. However, in time-domain simulations, this technique does not work properly. Some works have explored specifics PML implementations in time-domain simulations, see [42, 43]. COMSOL

does not recommend the PML approach to time-domain simulations [36]. To overcome this, we applied the "*Low-Reflecting Boundary*" at solid boundaries and a similar condition to the fluid, known as "*Plane Wave Radiation*". These boundary conditions are used in time domain simulations to reduce undesired reflections at boundaries. To avoid the presence of reflected waves at the detectors, which affect mainly the slower modes, we used large domains for fluids and solids, as shown in Table 4.1. The reduction in the amplitude of incoming and reflected waves is of order of 10^{-3}.

The pulse excitation, denoted by $q(t)$, is mandatory in time-domain simulations. Usually, Ricker wavelets are employed and will also be adopted here [44]. Mathematically, it is the second derivative of the Gaussian function. In the time domain, it is given by

$$q(t) = (1 - 2\pi^2 f_p^2 t^2) e^{-\pi^2 f_p^2 t^2} \tag{4.1.2}$$

where f_p is the central pulse frequency. Its spectrum, frequency domain, is given by

$$\hat{q}(\omega) = (\omega/\omega_p)^2 e^{-(\omega/\omega_p)^2} \tag{4.1.3}$$

where $\omega_p = 2\pi f_p$. The above expressions are plotted in Figure 4.2, considering $f_p = 8$kHz.

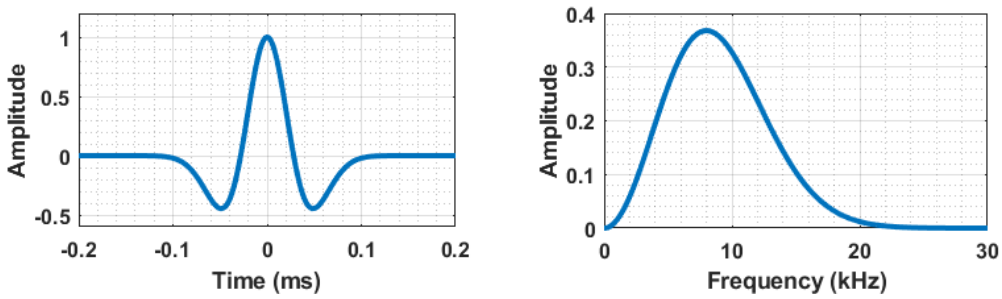

(a) (b)

Figure 4.2: Ricker wavelet representation with central frequency at 8kHz in (a) time-domain and (b) frequency domain.

The element size h was chosen to be ten times smaller than the most significant wavelength

$$h = \frac{v_{min}}{10\, f_p} \tag{4.1.4}$$

where v_{min} is the minimum value of propagating waves in the domain and f_p is the dominant frequency of the pulse. The domains are meshed using triangular elements. We discretized the time in 1024 equally spaced points from 0 ms to 5 ms.

To a direct comparison between modal analysis and time-domain results, we used the same elastic parameters. We note, however, that these parameters can be easily modified in both simulations. Elastic parameters used in the time domain studies are organized in Table 4.2.

Table 4.2: Parameters used during simulation for fast and slow formations. Fast formation considers fluid 1, whereas slow formation considers fluid 2.

Domain	S_p (µs/ft)	S_s (µs/ft)	ρ (kg/m^3)
Fluid 1	203.0	-	1000
Fluid 2	138.5	-	1000
Formation	87.0	152.4	2300

Figure 4.3(a) shows the resulting discretization map obtained for a fast formation using the conditions described above. The color scale presents the mesh element size distribution. Figure 4.3(b) shows a zoom in the interface, demonstrating the mesh parameterization according to the fluid or solid velocities, as well as the mesh resolution at the fluid-solid interface. Second-order shape functions in all domains were used.

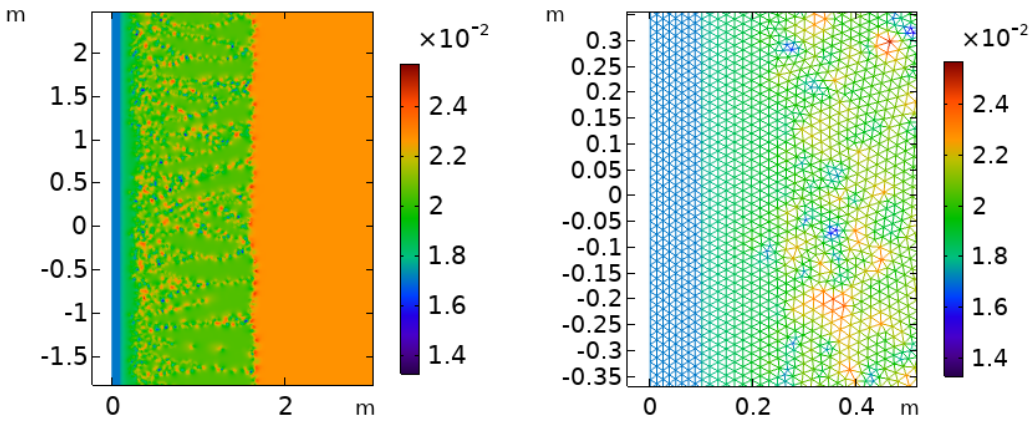

(a) (b)

Figure 4.3: (a) Discretization of the domains. Blue area indicated the mesh elements in the fluid. (b) Zoom near to solid-fluid interface. Color scale shows the mesh element size.

4.2 Data processing

In experiments, we only have access to signals recorded in time by the detectors. To obtain the modes dispersion curves, post-processing of the data is required. Therefore, before discussing the waveforms generated with our model, we briefly explain two processing algorithms that we employed in our analysis. One is based on the comparison of the waveforms detected in the time domain and the other on the analysis of the Fourier

transform of the signal in the frequency domain. The two algorithms were implemented by Dr. Pablo D. Batista. In both methods, the signal at i-th detector is labeled as $z_i(t)$ and its Fourier transform is labeled as $\hat{z}_i(f)$. The detectors are considered to be equally spaced by a distance d.

4.2.1 Slowness Time Coherence

The Slowness Time-Coherence (STC) is a post-processing algorithm based in the wave packet shape analysis in the time domain developed by Kimball in 1984 [2]. The algorithm uses a semblance (coherence) function that compares the waveforms between all the detectors. So, this algorithm can be only applied accurately to describe a non-dispersive wave. However, it can also be used to provide estimates of less intense waves. Dispersive waves can be processed more accurately by adding a Fourier transform analysis to the algorithm [37].

The output of STC is a coherence map where the arrivals in time of each mode can be observed for the different slowness (S) components of the wave packet. Considering N equally spaced detectors, and $\{z_1(t), ..., z_N(t)\}$ the registered signals, the semblance function $\rho^2(S,T)$ is given by

$$\rho^2(S,T) = \frac{\displaystyle\int_T^{T+T_w} \left| \sum_{i=1}^{N} z_i\left[t + Sd(i-1)\right] \right|^2 dt}{\displaystyle N \sum_{i=1}^{N} \int_T^{T+T_w} \left| z_i\left[t + Sd(i-1)\right] \right|^2 dt} \tag{4.2.1}$$

where T is the arrival time at the first detector and T_w is the size of the temporal window chosen to calculate the semblance. The back-propagation in time for the i-th detector is done by shifting the signal in time by the amount $Sd(i-1)$, which allows us to compare the waveforms (for a specific value of S) at each detector as if they were arriving at the same time. Besides, it is easy to see that the values of the coherence function are between 0 and 1, where the maximum value indicates that the waves are identical in shape and magnitude for all receivers. And, when there is no resemblance between the waveforms, the value of the function is zero. We point out that the STC version used here, which was written to treat experimental data, applies a Gaussian filter in the semblance matrix.

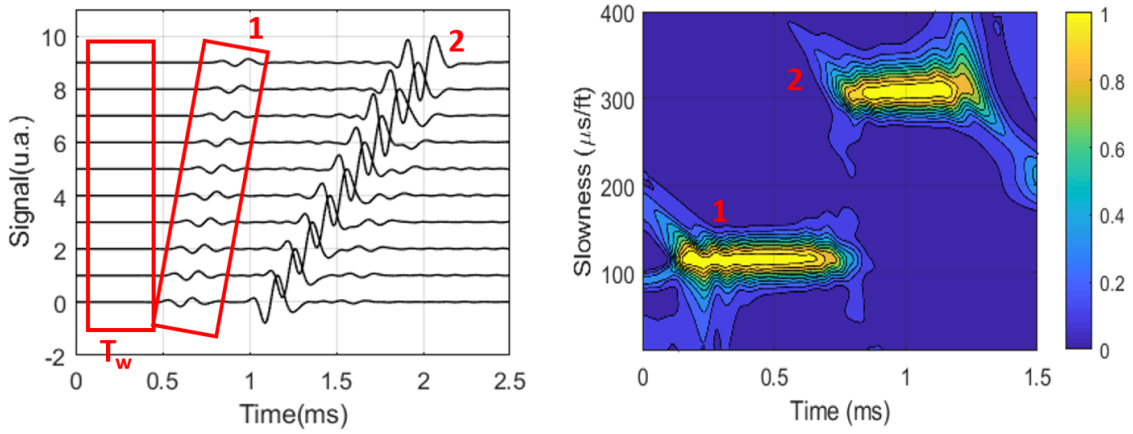

(a) (b)

Figure 4.4: Example of STC procedure: (a) Collected signals at detectors. The red rectangle represents a different interval of T_w in which the coherence, given by Equation 4.2.1, will be calculated. Its inclination is proportional to wave slowness. (b) Shows the processed coherence map for the recorded signal: two arrivals can be identified by the maximum coherence values.

Figure 4.4 illustrates the algorithm functioning. One can see the presence of two main modes labeled 1 and 2. The red rectangles represent the time windows for two different S values. By scanning the slowness and comparing the waveforms using Equation 4.2.1, the algorithm determines the S values which maximize the semblance. The result is a 2D map with the slowness as a function of time, as shown in Figure 4.4(b). The produced map gives us information about the wave arrival time in the first detector and its slowness. Intense dispersion results in low semblance, whereas slight dispersion results in distorted formats, as observed mainly for wave 2 in Figure 4.4(b).

4.2.2 Phase-Based Dispersion Analysis

The Phase-Based Dispersion Analysis (PBDA) method was developed by Assous *et al.* in 2013 to deal with dispersive waves as a robust alternative to more computationally heavy algorithms [3]. The method considers that the phase velocity can be found using the phase obtained in the Fourier transform of each recorded signal. Denoting the Fourier transform of recorded signals in time by $\{\hat{z_1}(f), ..., \hat{z_1}(f)\}$, it is possible to access the frequency content of each signal, its amplitude $A_i(f)$ and the phase shift $\phi_i(f)$.

For each frequency that composes the packet. It is possible to calculate the phase slowness from the signal of two adjacent detectors as follows [3]:

$$S = \frac{1}{v} = K\frac{\Delta\phi}{360fd} \tag{4.2.2}$$

where $\Delta\phi$ is the phase difference between the two signals (in degrees), f the frequency under analysis measured in Hz, d is the distance between the detectors in meters, $K = 304878$ the conversion factor from s/m to µs/ft. If the first detector is taken as reference, there will be $(N-1)$ phase differences, and a graph of $\Delta\phi$ versus the channel number for each frequency can be made. A linear regression is made and the phase slowness is computed as follows:

$$S = \frac{1}{v} = K\,\frac{|Angular\ coefficient|}{360fd} \tag{4.2.3}$$

In this way, we are able to obtain the value of S for each frequency of the Fourier transform spectrum and plot the dispersion curve of the mode. It is important, however, to point out that the phase information needs to undergo corrections through processes known as phase unwrapping and aliasing in order to generate the correct values of $\Delta\phi$ from the Fourier Transform [3]. In addition, the only frequencies analyzed are multiples of F_s/M to $F_s/2$, where F_s is the signal sampling frequency and M the number of points.

A drawback of the PBDA method is that, if two or more modes are not separated in frequency, their dispersion curves cannot be distinguished appropriately. Therefore, the method works very well when a single mode is present or when one of the modes is much stronger than the others.

4.3 Results

We show a cross-section of the cylindrical borehole defined by our FEM modeling in Figure 4.5. We plot the normalized solid displacement and normalized pressure for different times after the excitation of the system with a Ricker pulse at t0.2ms . Positive pressure means compression, while negative pressure means expansion. Figure 4.5(a) shows the displacement and pressure fields soon after the pulse excitation at $t = 0.2$ ms. The source emits a pulse which propagates isotropically in the fluid until the borehole wall. Then, part of its energy is transmitted to the solid formation. At this moment, three waves are generated, but they are not completely separated in space even after $t = 0.5$ ms, as shown in Figure 4.5(b). After $t = 1.0$ ms, Figure 4.5(c) shows that the spacial separation becomes evident. The last plot, Figure 4.5(d) shows the moment when they are completely separated at $t = 1.5$ ms. The presence of shear (P), compressional (S), and Stoneley (St) waves are indicated.

Part of the energy is trapped inside the cylindrical waveguide and propagates along the z-direction. Part is lost to the formation. The Stoneley wave carries guided energy. P and S waves are bulk waves and propagate along the formation and also close to the fluid-solid interface. In the solid, close to the interface, they scatter, exciting again the

fluid. That is the reason they are noted in the recorded signals. Normal and quasi-normal reflections at the wall also take place during the process. These waves can be seen in the detectors after long times after the main modes arrive. Figure 4.5, together with the ray-tracing scheme provided in Figure 2.2(b), helps us to understand the pattern of signals recorded by the detectors.

In order to obtain the slowness of our wave trains and see at what happens in the frequency domain, we performed simulations of fast and slow formations to be verified by the STC and PBDA algorithms. STC was used to obtain the propagating wave slowness of S and P waves. PBDA was used to obtain the dispersion curve for Stoneley mode to a direct comparison with the previous computed modal analysis performed in Chapter 3.

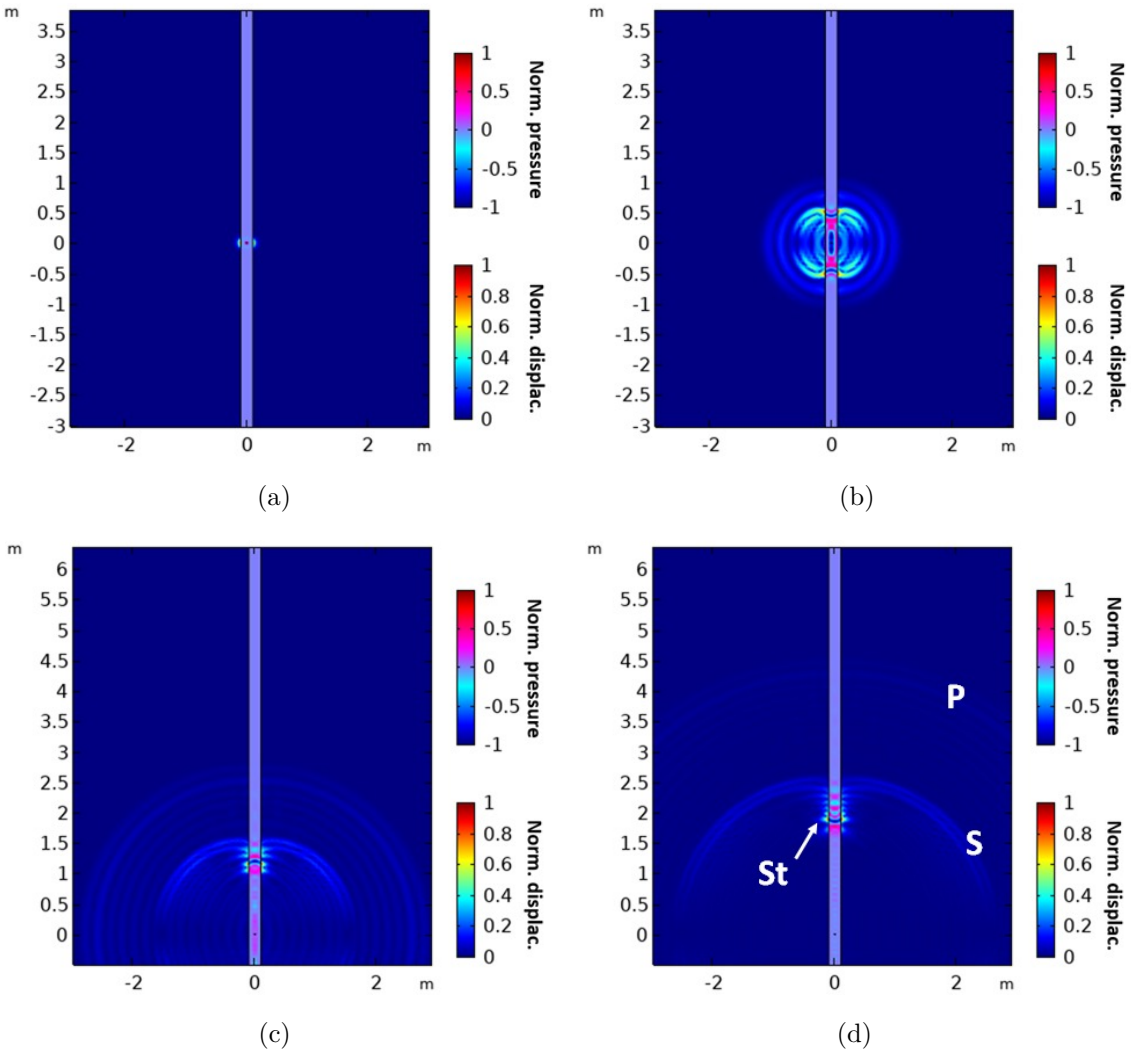

Figure 4.5: Wave packet evolution in our FEM model after excitation with a Ricker pulse at $z = 0$. The normalized solid total displacements and fluid pressures are plotter in four different times: (a) $t = 0.2$ ms (b) $t = 0.5$ ms (c) $t = 1.0$ ms (d) $t = 1.5$ ms. The presence of shear (P), compressional (S), and Stoneley (St) waves are indicated.

4.3.1 Waveforms

Figure 4.6(a) shows the waveforms detected at the 10 detectors in the time domain for the fast formation. Zoom in the signal of the first detector is shown in Figure 4.6(b) in order to highlight the weak P and S arrivals, where the presence of P and S waves can be noted. The energy is mainly concentrated in the Stoneley mode. Qualitatively, results are in agreement with expectations, since the presence of these three waves can be seen in a fast formation using the monopole source [8].

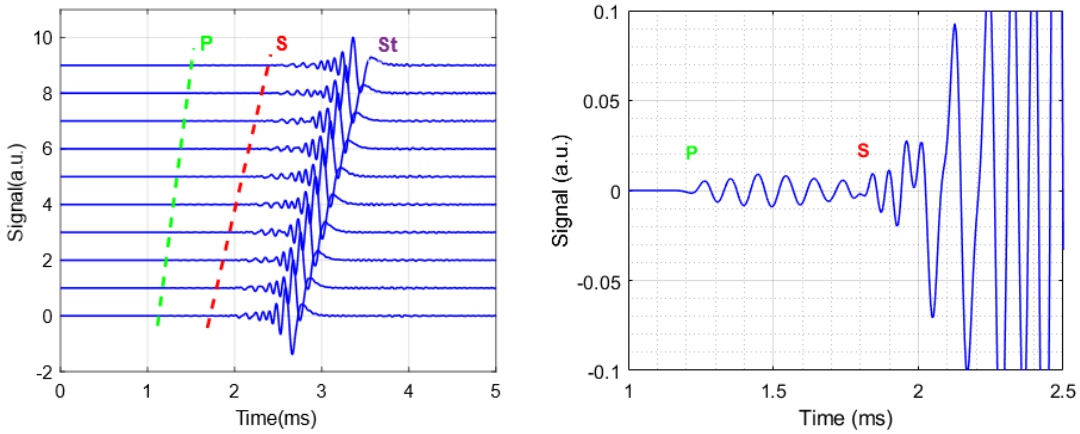

(a) (b)

Figure 4.6: Waveforms in a fast formation: (a) Signal amplitudes (in arbitrary units ($a.u.$)) obtained using the model and parameters presented in Section 4.1, using a Ricker wavelet centered in 8 kHz as excitation pulse. The arrival of each wave can be seen: compression (P) in green, shear (S) in red, and Stoneley (St) in purple. (b) Zoom in the first arrivals detected by the first detector in order to highlight the P and S arrivals.

Figure 4.7(a) shows the results obtained for the slow formation. Again, energy is concentrated in the guided Stoneley mode. A green dashed line is shown to indicate the P-wave arrival and zoom in the signal of the first detector is shown in Figure 4.7(b). A direct comparison between Figures 4.6(b) and 4.7(b) shows the P-wave arrival at the same time in the first detector for fast and slow formations. This occurs because this velocity depends only on the solid elastic parameters. Moreover, no signal of the S wave is evident, as expected from the discussion in Chapter 2 regarding the S wave propagating in slow formations.

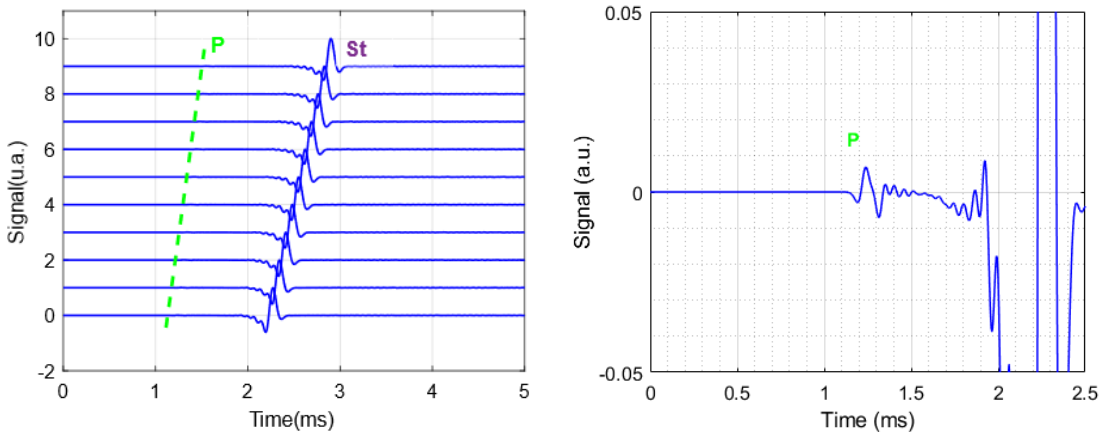

(a) (b)

Figure 4.7: Signals ($a.u.$) obtained in the slow formation by equally spaced detectors along time, given in ms, for the considered system using a Ricker wavelet centered in 8 kHz as excitation pulse. The arrival of each wave can be seen: compressional (P) in green, and Stoneley (St) in purple. (b) A zoom is provided in order to check the presence of less intense modes.

Figure 4.8(a) shows the coherence map for the fast formation obtained by applying the STC algorithm to the waveforms presented in Figure 4.6(a). One can see the presence of three regions of maximum coherence which start at different arrival times. They are attributed to the compressional, shear, and Stoneley arrivals. The corresponding apparent slowness of each of the modes is found using a maximum search and white dashed horizontal lines mark the corresponding values. Largely distorted regions in the coherence map indicate dispersive character, as observed in the Stoneley wave map in comparison to the compressional and shear maps.

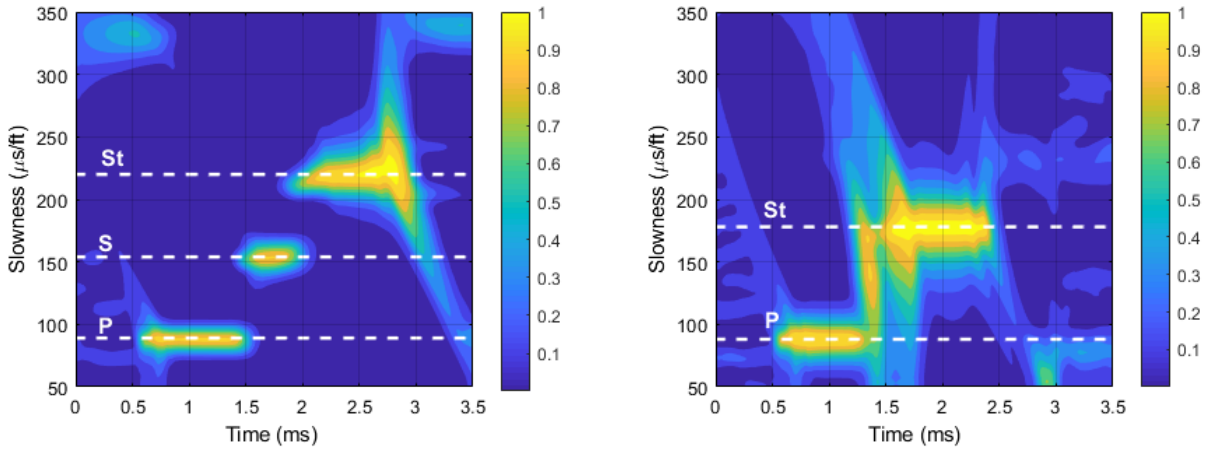

Figure 4.8: Coherence map obtained using the STC algorithm for: (a) fast formation and (b) slow formation using $T_w = 0.1$ ms. Coherent waves can be seen: S, P and St. The local maximum of each arrival is indicated in white dashed lines. The slowness is given in µs/ft and arrival time in ms.

Since the Stoneley mode is slightly dispersive, STC is not the best method to treat it. Therefore, Figure 4.9(a) shows in red dots the PBDA analysis for this mode. Differently from STC, PBDA provides a dispersion curve which starts around 226 µs/ft at low frequencies and slowly decays as the frequency increases. For comparison, in black solid line, we plot the dispersion obtained by applying the FEM modal analysis developed in Chapter 3. The agreement is very good for frequencies up to approximately 5 kHz, as highlighted on the inset, where both curves start to differ. The difference between both dispersions increases with frequency and some scattering is observed in the PBDA response around 11 kHz. Figure 4.9(b) shows the normalized Fourier transform of the signal acquired by the 10 detectors which are used in the PBDA processing. As we observe, at 5 kHz the Fourier transform reaches its maximum amplitude and starts to decay for higher frequencies. We attribute the gradual difference between the PBDA and the modal dispersion curves to aliasing effects that are not fully eliminated in the algorithm and affect the Fourier transform phase component. The scattering of points is most likely related to phase unwrapping [3]. The presence of internal reflections inside the borehole, which can add contribution at high frequencies to the signal detected in our time-domain model, may also have a contribution to this effect. Further tests will be performed to check these assumptions. However, the most important thing is that the PBDA and the modal analysis agree in a long range of frequencies, particularly in the low-frequency limit, which is as long as usual good signal-to-noise experimental data [4, 41, 45].

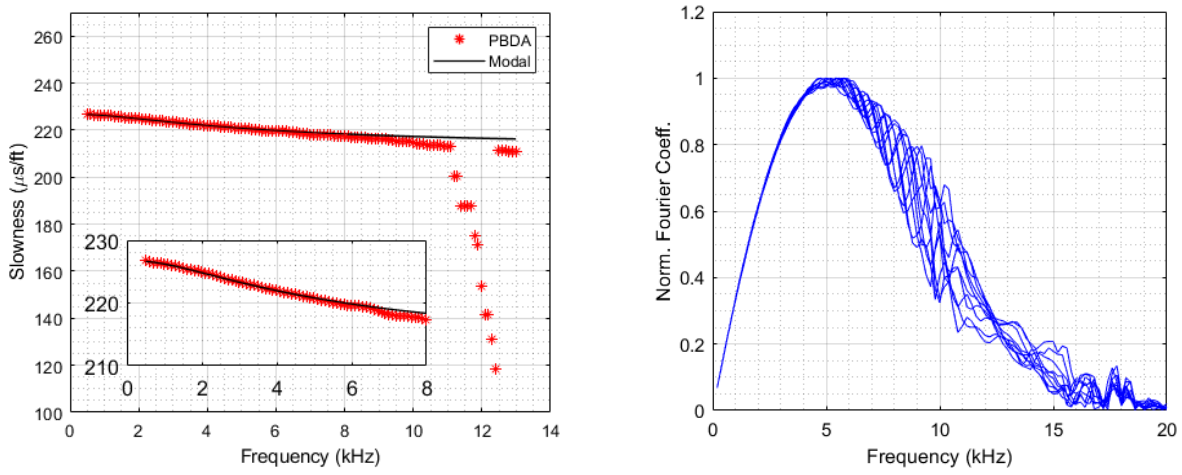

(a) (b)

Figure 4.9: Fast formation: (a) Comparison between the dispersion curves obtained using PBDA, in red asterisk, and using the modal analysis, in black continuous line, developed in Chapter 3. (b) Normalized Fourier transform of the signals at each detector.

Table 4.3 summarizes the low-frequency analysis of the fast formation of acoustic modes by comparing the different methods employed here. The column "Expected ($f = 0$)" reproduces the slowness of the P and S waves already presented in Table 4.2 with the addition of the low-frequency limit of the Stoneley wave obtained with Equation 3.2.2. The STC values for the P and S wave slowness are (88 ± 3) µs/ft and (153 ± 4) µs/ft. The uncertainties here are a rough estimate using the full width at half maximum in the flat regions (of slowness) for the two modes in Figure 4.8(a). The slowness values for S and P waves are in good agreement with the input of Table 4.2. The PBDA value for the Stoneley wave in the low-frequency limit is 227.7 µs/ft at 500 Hz, which is also a good comparison with the $f = 0$ value since the Stoneley mode shows a small plateau in the low-frequency limit. The Stoneley wave slowness obtained with our modal analysis presented in Chapter 3 calculated at 500 Hz is 226.6 µs/ft, thus demonstrating the agreement and consistency of our FEM time and frequency analysis.

Table 4.3: Comparison between FEM time and modal analysis for fast formation in the low-frequency limit. The expected slowness values for the time domain model are performed with STC and PBDA (at 500 Hz) algorithms. The column "Expected ($f = 0$)" presents the St wave slowness obtained with equation 3.2.2. The Modal analysis limit for the Stoneley wave slowness is calculated 500 Hz. Values of slowness are given in µs/ft.

Wave type	**Expected ($f = 0$)**	**STC**	**PBDA (500 Hz)**	**Modal (500 Hz)**
P	87.0	88 ± 3	-	-
S	152.4	153 ± 4	-	-
St	226.7	223 ± 8	227.7	226.6

The STC analysis of the slow formation is presented in Figure 4.8(b). As expected, the coherence map shows only the arrivals of the compressional and Stoneley waves. Figure 4.10(a) shows the dispersion curve for slow formation found applying the PBDA algorithm in red dots. We compare the post-processed data with the results from the modal analysis (black solid line). Again, the agreement is better below 6 kHz and the difference increases for higher frequencies. Figure 4.10(b) shows that the Fourier transform of the slow formation is slightly shifted to lower frequencies in comparison to the fast formation. In this case, small oscillations are present in the PBDA response even at lower frequencies. The difference (in %) as a function of the frequency between the slowness obtained with PBDA and our modal analysis for the two types of formation shown in Figure 4.11. Besides the good agreement in the low-frequency range, slow and fast formations dispersion curves obtained with PBDA show the same behavior in the high-frequency range.

The low-limit frequency analysis of the slow formation is organized in Table 4.4. Since the elastic parameters of the fast and slow formation are the same, the STC slowness of the P wave is quite similar to the same presented in Table 4.3. The slowness of the Stoneley mode at $f = 0$, obtained Equation 3.2.2 is 171.1 µs/ft. The PBDA value at 300 Hz of 169.8 µs/ft and is possibly affected by the oscillations already observed in Figure 4.10(a). From the FEM modal analysis, we obtain 171.4 µs/ft at 300 Hz, which is in very good agreement with the $f = 0$ limit. Again, we see a good agreement in the low-frequency values of the two modes obtained with the different approaches, once more validating our FEM time and frequency analysis.

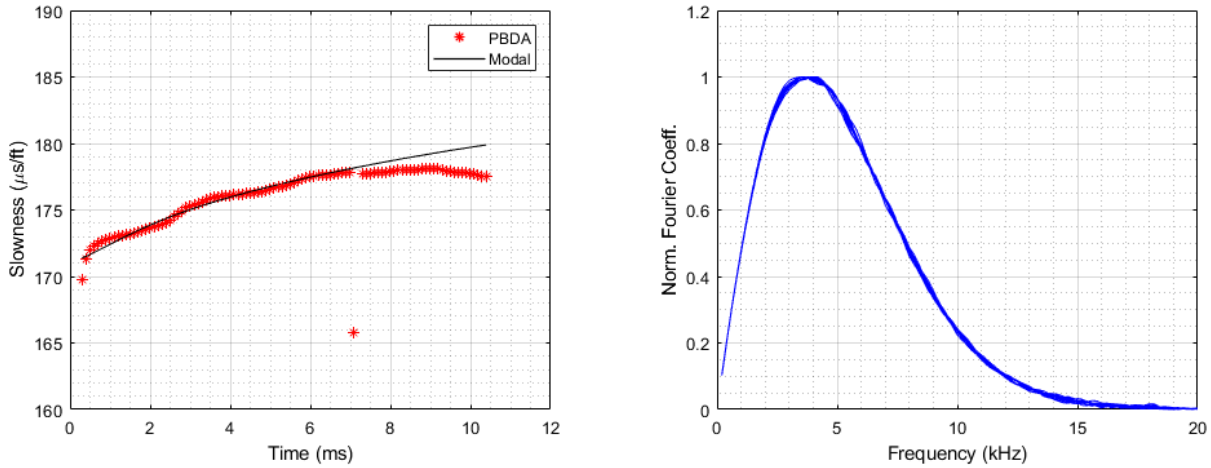

(a) (b)

Figure 4.10: Slow formation: (a) Comparison between dispersion curves obtained using PBDA, in red asterisk, and using the modal analysis, in black continuous line, for slow formation. (b) Normalized Fourier transform of the signals at each detector.

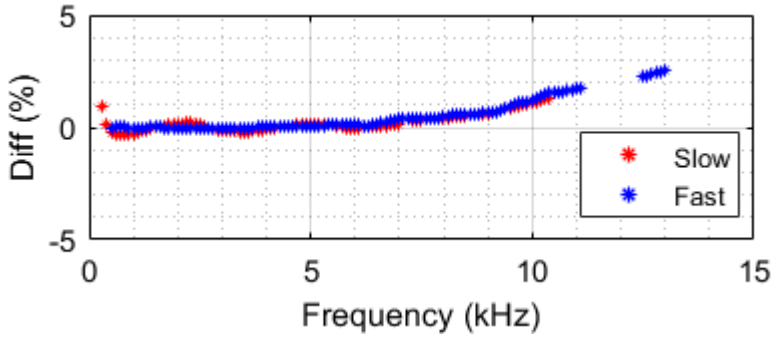

Figure 4.11: Percent difference between the slowness values obtained with PBDA and the modal analysis for the fast (blue dots) and slow formation (red dots).

Table 4.4: Comparison between FEM time and modal analysis for slow formation in the low-frequency limit. The expected slowness values for the time domain model are performed with STC and PBDA (at 300 Hz) algorithms. The column "Expected ($f = 0$)" presents the St wave slowness obtained with equation 3.2.2. The Modal analysis limit for the Stoneley wave slowness is calculated 300 Hz. Values of slowness are given in µs/ft

Wave type	**Expected ($f = 0$)**	**STC**	**PBDA (300 Hz)**	**Modal (300 Hz)**
P	87.0	87 ± 5	-	-
S	-	-	-	-
St	171.1	178 ± 9	169.8	171.4

Chapter 5

Conclusions and pespectives

We investigated some aspects of the Sonic logging technique using the Finite Element Method (FEM). We obtained a platform that allowed us to study an isotropic, homogeneous, and infinite borehole in the time and frequency domains.

With the modal analysis, we successfully obtained the dispersion curves for Stoneley, flexural, and screw modes for fast and slow formations. We validated our simulation by comparing our results with the first analytical description of the problem obtained for the Stoneley wave [9] and with a more general matrix formalism based solution for the three main guided modes [8]. We explored the physical interpretations of the dispersion curves of the modes and discussed how our simulation can be used to analyze them in the low-frequency limit. In this limit, the dispersion curves of post-processed time-domain data from experiments cannot be accurately determined due to its low signal-to-noise ratio. Our numerical simulations demonstrated to be reliable in frequencies up to 150 Hz, which is one order of magnitude lower than what is usually achieved in experimental data with reasonable signal to noise ratios.

The problem of a logging tool containing a monopole source was also addressed. To do so, a logging tool was simulated in the time domain with a Ricker pulse source which probes the fluid and formation. The signal is detected by N equally spaced detectors as in the real experimental situation. The detected waveforms were also analyzed in the cases of fast and slow formations. The analysis was performed with two different algorithms: the Slowness Time Coherence (STC) and the Phase-based Dispersion Analysis (PBDA). In the fast formation, we demonstrated the presence of P, S, and Stoneley waves, while in the slow formation only the P and Stoneley modes were present, as expected. For both types of formation, the comparison between the dispersion curves obtained with the post-processed data and with the modal analysis were in very good agreement, demonstrating the equivalence of our time and frequency FEM models.

In this way, we successfully developed a reliable platform for FEM calculation of the acoustic properties of modes in ideal fluid-filled boreholes. Our platform has the potential to receive further implementations which will increase the complexity of the

problems that it can deal with and, mainly, improve its applicability in real data analysis. Concentric solid layers, the presence of a physical tool (with elastic parameters), and in-plane anisotropies can be easily implemented in this platform. However, tools containing dipole or quadrupole sources will probably need full 3D calculations, which shall require more computation efforts.

References

1. Donaldson, E. Well logging for earth scientists. *Journal of Petroleum Science and Engineering.* ISSN: 09204105 (1989).
2. Kimball, C. V. & Marzetta, T. L. Semblance processing of borehole acoustic array data. *Geophysics.* ISSN: 00168033 (1984).
3. Assous, S., Linnett, L. & Elkington, P. *Phase-based dispersion analysis of borehole acoustic logs* in *Proceedings of Meetings on Acoustics* (2013).
4. Haldorsen, J. B. U. *et al.* Borehole Acoustic Waves. *Oilfield Review,* 34–43 (2006).
5. Alford, J. *et al. Sonic logging while drilling-shear answers* 2012.
6. Schmitt, D. P. *Multipole logging (radially layered) in transversely isotropic poroelastic formations* in *1989 SEG Annual Meeting* (1989).
7. Ma, J., Matuszyk, P. J., Mallan, R. K., Torres-Verdín, C. & Voss, B. C. *Joint processing of forward and backward extended prony and weighted spectral semblance methods for robust extraction of velocity dispersion data* in *SPWLA 51st Annual Logging Symposium 2010* (2010).
8. Tang, X. M. & Cheng, A. *Quantitative Borehole Acoustic Methods, Volume 24* 1st ed., 274. ISBN: 9780080440514 (2004).
9. Biot, M. A. Propagation of elastic waves in a cylindrical bore containing a fluid. *Journal of Applied Physics.* ISSN: 00218979 (1952).
10. Kurkjian, A. L. & Chang, S. K. Geometric decay of the headwaves excited by a point force in a fluid-filled borehole. *Geophysics* (1983).
11. Kurkjian, A. L. & Chang, S. K. Acoustic multipole sources in fluid boreholes. *Geophysics.* ISSN: 00168033 (1986).
12. Sinha, B. K. & Simsek, E. *Sonic logging in deviated wellbores in the presence of a drill collar* in *Society of Exploration Geophysicists International Exposition and 80th Annual Meeting 2010, SEG 2010* (Society of Exploration Geophysicists, 2010), 553–557. ISBN: 9781617389801.
13. Sinha, B. K., Norris, A. N. & Shu-Kong Chang. Borehole flexural modes in anisotropic formations. *Geophysics.* ISSN: 00168033 (1994).

14. Muga, I., Pardo, D., Matuszyk, P. J. & Torres-Verdín, C. Semi-analytical response of acoustic logging measurements in frequency domain. *Computers and Mathematics with Applications.* ISSN: 08981221 (2015).

15. Wang, T. & Tang, X. Finite-difference modeling of elastic wave propagation: A nonsplitting perfectly matched layer approach. *Geophysics* **68,** 1749–1755. ISSN: 00168033 (2003).

16. Jørgensen, O. & Burns, D. Novel finite-element approach applied to borehole quadrupole dispersion analysis in stress-sensitive formations. *Geophysics* **78.** ISSN: 00168033 (2013).

17. Liu, L., Lin, W. J., Zhang, H. L. & Wang, X. M. A numerical investigation of the acoustic mode waves in a deviated borehole penetrating a transversely isotropic formation. *Science China: Physics, Mechanics and Astronomy* **58.** ISSN: 16747348 (Aug. 2015).

18. Pardo, D. *et al.* Simulation of wireline sonic logging measurements acquired with Borehole-Eccentered tools using a high-order adaptive finite-element method. *Journal of Computational Physics* **230,** 6320–6333. ISSN: 10902716 (2011).

19. Pardo, D. *et al.* Influence of borehole-eccentred tools on wireline and logging-while-drilling sonic logging measurements. *Geophysical Prospecting.* ISSN: 00168025 (2013).

20. Matuszyk, P. J., Torres-Verdín, C. & Pardo, D. Frequency-domain finite-element simulations of 2D sonic wireline borehole measurements acquired in fractured and thinly bedded formations. *Geophysics* **78.** ISSN: 00168033 (2013).

21. Matuszyk, P. J. & Torres-Verdín, C. Frequency-domain simulation of logging-while-drilling borehole sonic waveforms. *Geophysics.* ISSN: 19422156 (2014).

22. *Sonic Scanner Schlumberger: Modular Sonic Imaging Platform* https://www.slb.com/.

23. Schmitta, D. P. Shear wave logging in elastic formations. *Journal of the Acoustical Society of America.* ISSN: NA (1988).

24. Aki, K. & Richards, P. G. *Quantitative Seismology* 2nd ed. (ed University Science Books) 700. ISBN: 1891389637 (2002).

25. Pujol, J. *Elastic Wave Propagation and Generation in Seismology* ISBN: 9780521817301 (Cambridge University Press, May 2003).

26. Auld, B. *Acoustic fields and waves in solids* ISBN: 0894644904 (1975).

27. Kausel, E. *Fundamental Solutions in Elastodynamics : a Compendium* 260. ISBN: 9780511546112 (Cambridge University Press, 2006).

28. Cheng, N., Cheng, C. H. & Toks6z, M. N. *Borehole wave propagation in three dimensions* tech. rep. (1994).

29. Liu, Q.-H. *et al. A three-dimensional finite difference simulation of sonic logging* tech. rep. (1996).

30. Sinha, B. K., Şimşek, E. & Liu, Q. H. Elastic-wave propagation in deviated wells in anisotropic formations. *Geophysics* **71.** ISSN: 00168033 (2006).

31. White, J. E. & Zechman, R. E. Computed response of an acoustic logging tool. *Geophysics* **33,** 229–392 (1968).

32. Tongtaow, C. *Wave propagation along a cylindrical borehole in a transversaly isotropic medium* PhD thesis (Colorado School of Mines, 1986).

33. Cheng, H. C. & Toksiiz, M. N. Elastic wave propagation in a fluid-filled borehole and synthetic acoustic logs. *Geophysics* **46,** 972–1061.

34. Gaede, O., Karpfinger, F., Jocker, J. & Prioul, R. Comparison between analytical and 3D finite element solutions for borehole stresses in anisotropic elastic rock. *International Journal of Rock Mechanics and Mining Sciences* **51,** 53–63. ISSN: 13651609 (Apr. 2012).

35. Liu, Q.-H. & Tao, J. The perfectly matched layer for acoustic waves in absorptive media. *Acoustical Society of America* **102** (1997).

36. *COMSOL Multiphysics® v. 5.4. www.comsol.com. COMSOL AB, Stockholm, Sweden* www.comsol.com.

37. Kimball, C. V. Shear slowness measurement by dispersive processing of the borehole flexural mode. *Geophysics.* ISSN: 00168033 (1998).

38. Paillet, L. F. & Cheng, H. C. *Acoustic Waves in Boreholes* 1st ed., 284. ISBN: 978-0849388903 (1991).

39. Rama Rao, V. N. & Vandiver, J. K. Acoustics of fluid-filled boreholes with pipe: Guided propagation and radiation. *The Journal of the Acoustical Society of America.* ISSN: 0001-4966 (1999).

40. Båth, M. *Mathematical Aspects of Seismology: Developments in Solid Earth Geophysics* 1st ed., 428. ISBN: 978-1483251103 (Elsevier, Jan. 1968).

41. Lee, S. Q., Tang, X. M., Su, Y. D. & Zhuang, C. X. Model-based dispersive processing of borehole dipole wave data using an equivalent-tool theory. *Geophysics.* ISSN: 19422156 (2016).

42. Assi, H. *Time-domain modeling of elastic and acoustic wave propagation in unbounded media, with application to metamaterials* PhD thesis (University of Toronto, 2016).

43. Mahmoud, A. R., Rattanawangcharoen, N., Luo, Y. & Wang, Q. FE-PML modeling of 3D scattering of transient elastic waves in cracked plate with rectangular cross section. *International Journal of Structural Stability and Dynamics* **10,** 1123–1139 (Dec. 2010).

44. Wang, Y. Frequencies of the Ricker wavelet. *Geophysics.* ISSN: 19422156 (2015).

45. Tang, X. M., Wang, T. & Patterson, D. Multipole acoustic logging-while-drilling. *SEG Technical Program Expanded Abstracts* **21,** 364–367. ISSN: 19494645 (Jan. 2002).

46. Huang, C. & Chen, L. *Negative Poisson's Ratio in Modern Functional Materials* 2016.

47. Kausel, E. *Fundamental Solutions in Elastodynamics* ISBN: 9780511546112 (Cambridge University Press, Cambridge, 2006).

Appendix A

Bulk waves and elastic parameters

The elastodynamic equation for homogeneous medium in the absence of external stresses is:

$$\rho \frac{\partial^2 u_i}{\partial t^2} = \sum_{jkl} \frac{\partial}{\partial x_j} \left(C_{ijkl} \frac{\partial u_k}{\partial x_j} \right), \quad i = 1, 2, 3 \tag{A.0.1}$$

A plane wave propagating in unbounded system can be described as

$$\mathbf{u}(\mathbf{x}, t) = \mathbf{A}\, e^{i(\mathbf{k}\cdot\mathbf{x} - wt)} \tag{A.0.2}$$

where $\mathbf{A} = (A_i, A_j, A_k)$ describes the wave polarization, $\mathbf{k} = (k_i, k_j, k_k)$ the direction of propagating wave and ω the angular frequency. Applying equation A.0.2 in equation A.0.1 leads to :

$$\left[\sum_{jkl} C_{ijkl} A_k k_k k_j - \rho \omega^2 A_i \right] e^{i(\mathbf{k}\cdot\mathbf{x} - wt)} = 0 \tag{A.0.3}$$

Dividing by $\rho|k|^2$, and noticing that $c^2 = \omega^2/|k|^2$, the equation can be written, using the directional cosines n_i, as

$$\sum_k \left[\sum_{jl} C_{ijkl} \frac{n_k n_j}{\rho} - c^2 \delta_{ik} \right] A_k e^{i(\mathbf{k}\cdot\mathbf{x} - wt)} = 0 \tag{A.0.4}$$

For isotropic solids the stiffness tensor is given by:

$$C_{ijkl} = \lambda \delta_{ij} \delta_{kl} + \mu(\delta_{ik}\delta_{jl} + \delta_{il}\delta_{jk}) \tag{A.0.5}$$

where λ and μ are the Lamé parameters. Taking equation A.0.5 into equation A.0.4:

$$\sum_{ki}\left[\left(\frac{\lambda+\mu}{\rho}\right)n_i n_k+\left(\frac{\mu}{\rho}-c^2\right)\delta_{ik}\right]A_k=0 \tag{A.0.6}$$

so, the following system needs to be solved

$$\begin{bmatrix}\left(\frac{\lambda+\mu}{\rho}\right)n_1n_1+\left(\frac{\mu}{\rho}-c^2\right) & \left(\frac{\lambda+\mu}{\rho}\right)n_1n_2 & \left(\frac{\lambda+\mu}{\rho}\right)n_1n_3\\ \left(\frac{\lambda+\mu}{\rho}\right)n_2n_1 & \left(\frac{\lambda+\mu}{\rho}\right)n_2n_2+\left(\frac{\mu}{\rho}-c^2\right) & \left(\frac{\lambda+\mu}{\rho}\right)n_2n_3\\ \left(\frac{\lambda+\mu}{\rho}\right)n_3n_1 & \left(\frac{\lambda+\mu}{\rho}\right)n_3n_2 & \left(\frac{\lambda+\mu}{\rho}\right)n_3n_3+\left(\frac{\mu}{\rho}-c^2\right)\end{bmatrix}\begin{bmatrix}A_1\\A_2\\A_3\end{bmatrix}=\begin{bmatrix}0\\0\\0\end{bmatrix} \tag{A.0.7}$$

To have non-trivial solutions, the determinant needs to vanish. Since the medium is isotropic, a direction can be chosen without losing generality. Considering $\mathbf{n}=(1,0,0)^T$, the values of phase velocities c (eigenvalues) can are:

$$c_1^2=\frac{2\mu+\lambda}{\rho}\qquad c_2^2=\frac{\mu}{\rho} \tag{A.0.8}$$

Using equation A.0.8 into A.0.6, the components of $\mathbf{A}$ can be calculated and is trivial to conclude that:

$$\begin{aligned}c_2^2&=\frac{\mu}{\rho}\Rightarrow\mathbf{A}\perp\mathbf{n}\\ c_1^2&=\frac{\lambda+2\mu}{\rho}\Rightarrow\mathbf{A}\parallel\mathbf{n}\end{aligned} \tag{A.0.9}$$

The above conditions imply that the propagating wave can be decomposed in two different polarizations: perpendicular and parallel to the propagating direction. This is the reason c_1 and c_2 are recognized as compressional (v_p) and shear (v_s) velocities. These results are independent of the coordinate system.

Isotropic and homogeneous media is completely described using these two parameters. The relation among most used elastic parameters are organized in Table A.1, where we can see how the first and second Lamé parameters are related to the Young modulus and Poisson ratio denote by E and ν, respectively. Table A.1 also shows how v_p and v_s can be written in therms of these different elastic parameters.

The second Lamé parameter, also called the shear modulus, is the relation between the shear strain and shear stress. It is the resistance of a material to shear stresses. Generally, fluids do not support shear, implying $\mu=0$. The first Lamé parameter doesn't have a direct physical interpretation as the Poisson ratio and Young modulus.

The Young Modulus is interpreted as the proportionality constant between strain and stress in an uniaxial direction. The Poisson ratio measures the deformation between

two perpendicular directions in solids. Mathematically, when the load is applied in the z-direction, it can be described as the ratio of the two strain components

$$\nu = -\frac{e_{xx}}{e_{zz}}, \tag{A.0.10}$$

the negative sign is for compensating the stretching in one direction and compression in another. Generally, ν is positive but, recently, materials have been designing to have negative values for the Poisson ratio [46].

Table A.1: Relation between different elastic parameters. Adapted from [1]

	λ, μ	E, ν	ρ, v_p^2, v_s^2
λ	λ	$\frac{E\nu}{(1+\nu)(1-2\nu)}$	$\rho(v_p^2 - 2v_s^2)$
μ	μ	$\frac{E}{2(1+\nu)}$	ρv_s^2
E	$\frac{\mu(3\lambda+2\mu)}{\lambda+\mu}$	E	$\frac{\rho v_s^2(3v_p^2-4v_s^2)}{v_p^2-v_s^2}$
ν	$\frac{\lambda}{2(\lambda+\mu)}$	ν	$\frac{v_p^2-2v_s^2}{2(v_p^2-v_s^2)}$
v_p^2	$\frac{\lambda+2\mu}{\rho}$	$\frac{E(1-\nu)}{\rho(1+\nu)(1-2\nu)}$	v_p^2
v_s^2	$\frac{\mu}{\rho}$	$\frac{E}{\rho 2(1+\nu)}$	v_s^2

In anisotropic media, equation A.0.4 can be used just replacing the correspondent stiffness tensor. In this case, shear wave degeneracy is usually broken, giving rise to two shear waves referred as qSV and qSH. More considerations about different anisotropic mediums can be found in [47].